1 **Orbital Evidence for Clay and Acidic Sulfate Assemblages on Mars Based on**
2 **Mineralogical Analogs from Rio Tinto, Spain**
3
4 Hannah H. Kaplan[1]*, Ralph E. Milliken[1], David Fernández-Remolar[2], Ricardo Amils[3],
5 Kevin Robertson[1], and Andrew H. Knoll[4]
6
7 Authors:
8
9 [1] Department of Earth, Environmental and Planetary Sciences, Brown University,
10 Providence, RI, 02912 USA.
11
12 [2]British Geological Survey, Nicker Hill, Keyworth, NG12 5GG, UK.
13
14 [3] Centro de Astrobiologia (INTA-CSIC), Ctra Ajalvir km 4, Torrejon de Ardoz, 28850,
15 Spain.
16
17 [4] Department of Organismic and Evolutionary Biology, Harvard University,
18 Çambridge, MA, USA.
19
20 *Corresponding author: Hannah_Kaplan@Brown.edu

Abstract

Outcrops of hydrated minerals are widespread across the surface of Mars, with clay minerals and sulfates being commonly identified phases. Orbitally-based reflectance spectra are often used to classify these hydrated components in terms of a single mineralogy, although most surfaces likely contain multiple minerals that have the potential to record local geochemical conditions and processes. Reflectance spectra for previously identified deposits in Ius and Melas Chasma within the Valles Marineris, Mars, exhibit an enigmatic feature with two distinct absorptions between 2.2 – 2.3 µm. This spectral 'doublet' feature is proposed to result from a mixture of hydrated minerals, although the identity of the minerals has remained ambiguous. Here we demonstrate that similar spectral doublet features are observed in airborne, field, and laboratory reflectance spectra of rock and sediment samples from Rio Tinto, Spain. Combined visible-near infrared reflectance spectra and X-ray diffraction measurements of these samples reveals that the doublet feature arises from a mixture of Al-phyllosilicate (illite or muscovite) and jarosite. Analyses of orbital data from the Compact Reconnaissance Imaging Spectrometer for Mars (CRISM) shows that the martian spectral equivalents are also consistent with mixtures of Al-phyllosilicates and jarosite, where the Al-phyllosilicate may also include kaolinite and/or halloysite. A case study for a region within Ius Chasma demonstrates that the relative proportions of the Al-phyllosilicate(s) and jarosite vary within one stratigraphic unit as well as between stratigraphic units. The former observation suggests that the jarosite may be a diagenetic (authigenic) product and thus indicative of local pH and redox conditions,

45   whereas the latter observation may be consistent with variations in sediment flux

46   and/or fluid chemistry during sediment deposition.

47

48   **Key points:**
49   • A doublet absorption is observed in reflectance spectra of Mars between 2.2 -
50   2.3 µm.
51   • Reflectance spectra at Rio Tinto, Spain also show a doublet due to Al-
52   phyllosilicate and jarosite.
53   • Spectral variation in martian deposits suggests local variation in pH, redox,
54   and/or sediment flux.
55
56
57   **Keywords:** Mars, surface; Spectroscopy; Infrared observations
58

1. Introduction

Outcrops of sulfate and clay mineral-bearing rocks are widespread across the ancient surface of Mars [Bibring et al., 2006; Murchie et al., 2009; Ehlmann et al., 2011; Carter et al., 2013], indicating that a complex history of water-rock interaction is preserved in the martian rock record. Visible-near infrared (VIS-NIR) reflectance spectra acquired by the CRISM (Compact Reconnaissance Imaging Spectrometer for Mars) and OMEGA (Observatoire pour la Minéralogie, l'Eau, les Glaces et l'Activité) imaging spectrometers have been used to identify clay minerals in ancient and heavily cratered Noachian terrains [Poulet et al., 2005; Ehlmann et al., 2011; Carter et al., 2013] and thick deposits of sulfates in younger Hesperian terrains and basins [Gendrin et al., 2005; Bibring et al., 2006]. In the cases of Terra Meridiani, Gusev Crater, and Gale Crater, these minerals have been examined *in situ* by rover-based payloads, providing detailed local geologic context for some of these orbital detections [e.g. Klingelhofer et al., 2004; Squyres et al., 2004; Arvidson et al., 2008; Wang et al., 2006; Vaniman et al., 2014].

Many of these orbiter-based detections of hydrated minerals on Mars are discussed in terms of single minerals. That is, the reflectance spectra of these deposits are commonly discussed or interpreted as specific clay, sulfate, or other hydrated minerals (see Ehlmann et al., 2009 for an exception with regards to mineral assemblages at Nili Fossae). Though these deposits are undoubtedly polymineralic, it appears that in many cases a single mineral can be *spectrally* dominant even at the spatial resolution of instruments such as CRISM (e.g., ~18

82   m/pixel). Therefore, those regions on Mars whose reflectance spectra cannot clearly

83   be attributed to a single dominant hydrated mineral are of particular interest as

84   they may record different and more diverse geological processes than are typically

85   recognized from CRISM data.

86

87   Reflectance spectra of deposits and strata within the Valles Marineris reveal

88   a number of locations that fall within this category, and these are the focus of this

89   study. Specifically, CRISM spectra of various deposits within Ius, Melas, and other

90   chasmata exhibit an absorption feature with local minima centered at ~2.21 and

91   ~2.27 μm [Metz et al., 2009; Roach et al., 2010; Weitz et al., 2011] (Figure 1). The

92   spectral shape and properties of this absorption feature, which we will refer to as a

93   spectral 'doublet', does not match the spectrum of any single common mineral in

94   existing spectral libraries, suggesting it likely cannot be attributed to a single type of

95   clay, sulfate, or other common hydrated mineral.

96

97   Previous studies have hypothesized that this material represents a mixture

98   of clays, sulfates (possibly including jarosite), and/or poorly crystalline phases

99   [Roach et al., 2010; Tosca et al., 2008b; Noe Dobrea et al., 2011; Weitz et al., 2014],

100   but the exact assemblage remains unknown. We have observed that similar spectral

101   features occur in airborne, field, and lab spectra of rocks and sediments at Rio Tinto,

102   Spain, which has been previously studied as a Mars analog due to the river's acidity,

103   iron hydrochemistry, and extensive iron oxide deposits [Fernandez-Remolar et al.

104   2003]. Indeed, it has been suggested that the ferric iron and sulfate mineralogy

105   produced by the acidic waters may be analogous to conditions experienced in Terra

106   Meridiani during the Hesperian [Fernandez-Remolar et al., 2004], and similar

107   conditions may also have occurred in portions of the Valles Marineris [e.g., Bibring

108   et al., 2007].

109

110   In this study we integrate airborne, *in situ*, and lab measurements to

111   characterize a suite of samples from different sites at Rio Tinto to understand the

112   mineralogical origin of the 'doublet' spectral signature, and we then compare our

113   findings to reflectance spectra acquired by the CRISM instrument for deposits in

114   Valles Marineris, Mars. We demonstrate that the doublet absorptions observed in

115   samples from Rio Tinto are comparable to the spectral signatures observed in Valles

116   Marineris, that the former are the result of Al-bearing phyllosilicates mixed with

117   jarosite, and that similar mineral assemblages may be present on Mars. This

118   indicates Rio Tinto contains materials that can serve as mineralogical and spectral

119   analogs for the martian deposits, though the geological processes that lead to the

120   formation of these assemblages on Earth and Mars need not be equivalent.

121   Specifically, although jarosite and Al-phyllosilicates may co-occur in geologic units

122   today on Mars, this association does not require their formation environments to

123   have been the same in space and/or time. Both mineral types may be authigenic or

124   detrital, and detailed geologic context is necessary to distinguish between these

125   options and the associated implications for local paleoenvironmental conditions.

126

127   **2. Background**

128   *2.1 Overview of Clay and Sulfate Detections on Mars*

129   The most commonly observed spectral signatures on Mars that have been

130   interpreted as clay minerals are identified as Fe/Mg smectite, but mixed-layer clays,

131   chlorite, Al-smectite, mica, kaolinite, and serpentine have also been observed

132   [Mustard et al., 2008; Murchie et al., 2009; Ehlmann et al., 2011; Carter et al., 2013].

133   Aqueous alteration of basaltic protoliths both at the surface and in the subsurface

134   have been invoked as the major source of these clay minerals, although subsequent

135   erosion and eolian/fluvial transport has led to their occurrence in a number of

136   different depositional environments. Intriguingly, these clay minerals, hereafter

137   referred to simply as 'clays', occur predominantly in terrains that are Noachian

138   (>3.6 Ga) in age [Bibring et al., 2006]. The presence and apparent spatial and

139   temporal distribution of these clays has been used to infer that early Mars was

140   characterized by circum-neutral pH, low salinity, and possibly habitable conditions

141   [Ehlmann et al., 2011]. More recently, *in situ* observations of clay-bearing

142   mudstones in Gale Crater by the Curiosity rover are also supportive of a habitable

143   environment, possibly during the Hesperian [Grotzinger et al., 2014; 2015; Vaniman

144   et al., 2014; Bristow et al., 2015].

145

146   In contrast, sulfate detections on Mars typically occur in younger Hesperian

147   terrains and may be indicative of a decreased hydrological cycle [Bibring et al.,

148   2006]. Decreased water availability, coupled with increasing salinity, may indicate

149   near-surface conditions inhospitable to most life [e.g., Tosca et al., 2008a]. Though

150   many sulfate salts (e.g., Ca, Na, and Mg-sulfates) can form under a wide range of pH

151   conditions, it is worth noting that Al^{3+} and Fe^{3+}-sulfates are indicative of low-pH

152   fluids. As such, understanding the distribution and geologic setting of these minerals

153   on Mars has important implications for deciphering ancient aqueous chemistry,

154   whether it be indicative of surface waters, groundwater, or diagenetic fluids.

155

156   Jarosite, a ferric sulfate that forms under acidic conditions and that was first

157   detected on Mars by the Opportunity Rover in Meridiani Planum [Squyres et al.,

158   2004], has received considerable attention in this context. Integrated payload

159   observations by the rover reveal that jarosite is likely associated with Mg and Ca-

160   sulfates at this location, all of which occur in eolian sandstones that have been

161   interpreted as reworked dune and playa sediments [Grotzinger et al., 2005]. The

162   Curiosity rover has also detected small amounts of jarosite in clay-bearing

163   laminated mudstones in Gale Crater [Cavanagh et al., 2015], though the origin of this

164   phase (e.g., detrital or authigenic) in these deposits is not yet well constrained.

165

166   Orbital observations of jarosite and other possible ferric sulfates have also

167   been reported in the Mawrth Vallis, Aram Chaos, Noctis Labyrinthus, and Valles

168   Marineris regions of Mars [Bibring et al., 2007; Milliken et al., 2008; Farrand et al.,

169   2009; Metz et al., 2009; Lichtenberg et al., 2010; Weitz et al., 2010; Thollot et al.,

170   2011; Noe Dobrea et al., 2011]. Of the Valles Marineris detections, possible

171   submarine fan deposits in Melas Chasma and strata exposed on the surrounding

172   plains are notable in that ferric sulfates are found in proximity to other hydrated

173   minerals such as opaline silica, providing additional constraints on local aqueous

174   geochemistry [Milliken et al., 2008; Metz et al., 2009]. These rover- and orbiter-

175   based observations indicate ferric sulfates may be common alteration or diagenetic

176   phases on Mars, as discussed by Burns [1988; 1993], and understanding their

177   occurrence can provide insight into local, regional, or global redox conditions.

178

179   *2.2 CRISM Observations of the Spectral 'Doublet'*

180

181   CRISM spectra of martian deposits that exhibit the 'doublet' feature

182   mentioned above are characterized by absorption maxima (reflectance minima)

183   occurring at wavelengths of 2.205-2.218 and 2.265-2.278 µm. These spectral

184   features have been noted previously in a number of CRISM-based studies,

185   particularly for deposits within Valles Marineris, and in some of these studies the

186   material has been referred to as a hydrated silicate [e.g., Roach et al., 2010].

187   However, many minerals, including gypsum, jarosite, nontronite, and silica, exhibit

188   absorptions in this wavelength range, and it is possible that the spectral doublet

189   represents a mixture of two or more hydrated minerals (Figure 1). The main

190   doublet feature is consistent with vibrational absorptions due to the presence of

191   cation-OH bonds, although the position and shape of absorptions within the feature

192   lead to ambiguity in determining the specific cation(s). The shorter wavelength

193   absorption ($\sim$2.21 µm) may be consistent with Si- or Al-OH bonds, whereas the

194   longer wavelength feature ($\sim$2.27 µm) may be indicative of Fe- or Mg-OH bonds.

195   However, spectra of H_2O-bearing Ca-sulfates such as gypsum also exhibit

196 absorptions in this wavelength region, despite the lack of structural Si, Al, Fe, Mg, or

197 OH.

198

199 In addition, CRISM spectra that exhibit the doublet feature also exhibit an

200 absorption at ∼1.9 μm due to the combination stretch+bend vibration mode of H_2O.

201 A similar doublet absorption has also been observed in laboratory spectra of poorly

202 crystalline Fe-silicate and sulfate mixtures [Tosca et al., 2008b] as well as acid-

203 leached Fe-smectite [Madejova et al., 2009], suggesting the spectral signature may

204 also be consistent with poorly crystalline or amorphous phases. Therefore, while it

205 is likely that the spectral doublet feature is indicative of OH and/or H_2O-bearing

206 phases, the specific mineral assignments remain ambiguous.

207

208 Roach et al. [2010] proposed four hypotheses to explain the doublet

209 material: (1) a mixture of sulfates (in particular, sulfates structurally similar to

210 gypsum and jarosite), (2) a mixture of opaline silica and Fe/Mg-smectite, (3) an Al-

211 OH phase mixed with Fe/Mg-smectite and/or jarosite, and (4) acid-leached Fe/Mg-

212 smectite or neoformation of poorly crystalline clays. Subsequent study by Weitz et

213 al. [2014] supported the latter two hypotheses based on an analysis of CRISM

214 spectra for the Melas Chasma region, demonstrating that the spectral doublet is

215 associated with "light-toned draping deposits" (termed LD in Weitz et al., 2014) that

216 locally form some of the highest stratigraphic units. These LD deposits extend

217 through portions of Melas Chasma and drape over pre-existing topography,

218 suggesting an airfall origin. Weitz et al. [2014] interpreted this LD unit to have been

219   deposited after the Late Hesperian valleys that incise the walls of the chasma, but

220   stratigraphic position alone cannot be used to determine whether the hydrated

221   phase(s) associated with the spectral doublet in this unit represent transported

222   sediments or authigenic products.

223

224   Roach et al. [2010] described a similar thin light-toned unit in Ius Chasma

225   that drapes pre-existing topography, but the stratigraphic and possible genetic

226   relationships between this unit and those in Melas have not yet been established.

227   Roach et al. [2010] interpreted the light-toned unit to have been emplaced on top of

228   Fe/Mg-smectite and sulfate-bearing strata either during or after a period of acidic

229   aqueous alteration when sulfates formed from evaporating brines. Another study by

230   Weitz et al. [2011], of Noctis Labrynthis, identified the doublet material in a ~20 m-

231   thick massive light-toned unit that outcrops near the top of a stratified light-toned

232   deposit [see Weitz et al., 2011 Figure 2]. It was suggested that this deposit was also

233   formed under acidic conditions, and the doublet-bearing unit was interpreted to

234   pre-date deposition of Fe/Mg- smectite and sulfates in the same region [Weitz et al.,

235   2011]. Although the doublet-bearing materials in Valles Marineris are often

236   associated with units that drape pre-existing topography, including the canyon

237   wallrock, Metz et al. [2010] provided evidence for deformation features in some of

238   the deposits, suggesting they may have originated higher up the canyon walls than

239   indicated by their current topographic position. Finally, CRISM data for Mawrth

240   Vallis also show evidence for doublet-bearing materials in the vicinity of Fe/Mg-

241   smectites and Al-phyllosilicates [Noe Dobrea et al., 2011; Bishop et al., 2013].

242

243   To summarize, doublet-bearing units are present in stratigraphic sections

244   that contain hydrated minerals suggestive of complicated and extended periods of

245   water-rock interaction and/or sediment transport. Fe/Mg-smectites and sulfates are

246   often found in nearby units and in most cases these occur in strata emplaced prior

247   to the doublet-bearing units. An exception is Noctis Labrynthis, where the doublet

248   material occurs in a unit that lies stratigraphically below an Fe/Mg smectite-bearing

249   outcrop.

250

251   We note that jarosite, which typically forms under conditions of pH<4, is also

252   identified in several of the regions that also exhibit the spectral doublet [Milliken et

253   al., 2008, Metz et al., 2009, Noe Dobrea et al., 2011]. Although the jarosite deposits

254   are not necessarily in rocks that are stratigraphically adjacent to the doublet

255   materials, the presence of this mineral in these regions may provide insight into

256   local aqueous geochemistry. Jarosite deposits on Mars may have formed where

257   acidic sulfate-bearing water ponded and subsequently evaporated [Tosca and

258   McLennan, 2006], though it is also possible for jarosite to form through chemical

259   weathering of basalt [e.g., Madden et al., 2004]. Alternatively, acidic conditions that

260   lead to jarosite formation may be induced by local or regional oxidation of Fe^{2+}-

261   bearing fluids, possibly via the emergence of groundwater and interaction with the

262   oxidizing martian atmosphere [Hurowitz et al., 2009]. An important aspect of any of

263   these scenarios is that the presence of authigenic jarosite records information about

264   local pH as well as redox conditions.

265

266

267   *2.3 Overview of Field Region at Rio Tinto, Spain*

268   The headwaters of the Rio Tinto near Nerva, Spain are acidic (mean pH of

269   2.3) and rich in ferric iron and other heavy metals. Three terraces of the Rio Tinto

270   are exposed in the river valley with the youngest terrace closest in elevation to the

271   modern day channel and the intermediate and oldest terraces located

272   stratigraphically above it (see Figure 2). The youngest of these (called the lower or

273   young terrace) is Holocene in age (750-1500 years) and composed of poorly sorted

274   conglomerates overlain by cross-bedded sandstones. Both types of deposits are

275   consistent with formation by mass wasting and sediment accumulation in the active

276   channel, a process that also occurs in the modern river. The Pleistocene-aged (~35

277   Ky) intermediate terrace is exposed 100 m above the lower terrace and consists of

278   poorly sorted clasts of country rock within a goethite-bearing matrix; this terrace is

279   distinct from the other river terraces as it lacks the sedimentary facies

280   corresponding to channel and backwater deposits seen in both the young and old

281   terraces. Finally, the Late Pliocene-aged (2 My) upper or old terrace is exposed in a

282   ≥10m thick outcrop at Alto de la Mesa. The outcrop at Alto de la Mesa consists of a

283   lag conglomerate overlain by sandstones and iron oxide precipitates, reflecting

284   similar types of channel deposits as those seen in the lower terrace. Further

285   description of the terraces and radiometric age constraints are reported in

286   Fernández-Remolar and Knoll [2008].

287

288　　　　The mineralogy of the modern river system and its terraces is dominated by

289　　ferric oxides and ferric sulfates. A number of previous studies have investigated

290　　variations in the mineralogical assemblages in the river terraces using X-ray

291　　diffraction (XRD), visible-near infrared (VIS-NIR) reflectance spectroscopy, and

292　　Raman spectroscopy [Fernández-Remolar et al., 2005; Roach et al., 2006; Chemtob

293　　et al., 2006; Sobron et al., 2009, 2014,]. The reader is directed to Fernández-Remolar

294　　et al. [2005] for a more thorough discussion on the mineralogy and mineral-forming

295　　processes of the Rio Tinto. Those authors found that seasonal precipitation of Ca-

296　　and Fe-sulfates occurs near the source region of the river, with the Fe-sulfates

297　　jarosite (in particular hydronium jarosite), schwertmannite, and copiapite making

298　　up much of the mineral assemblage, along with nanophase iron oxide and

299　　nanophase goethite. Only the most stable minerals (iron oxides, goethite, jarosite)

300　　survive through the wet season, during which meteoric water dissolves many of the

301　　precipitates and aids in cementation of the terrace deposits. Jarosite is less

302　　abundant and often absent in the older deposits, likely due to its long-term

303　　instability under wet conditions, and these units instead contain more stable Fe-

304　　oxides such as goethite and hematite. Therefore, the persistence of jarosite may

305　　indicate a low degree of water-rock interaction or low water-to-rock ratios since its

306　　precipitation. Country rock in this region is composed of quartz, chlorite, and pyrite,

307　　which act as a source of solutes for the precipitates as well as a source of detritus for

308　　the terrace conglomerates.

309

310   In addition to sulfates and Fe-oxides, phyllosilicates (2M1 illite, chlorite,

311   kaolinite, and smectites) are also present throughout the Rio Tinto system and are

312   thought to form by alteration of the volcanosedimentary bedrock near the source of

313   the acidic river system [see Fernández-Remolar et al., 2011 for details]. At Rio Tinto,

314   phyllosilicates typically accumulate at times of maximum waterflow during the wet

315   season when deposition of detrital sediment is dominant over chemical

316   sedimentation, but they can also be found in environments where conditions are

317   outside those typical for clay formation, such as the low-pH source streams. The

318   diversity and stability of these phyllosilicates depends on the hydrology, source rock

319   composition and geochemical processes occurring in the river, all of which must be

320   accounted for when interpreting the deposits [Fernández-Remolar et al., 2011].

321   Likewise, jarosite is neither stable nor formed in all of Rio Tinto's hydrogeochemical

322   environments [Fernández-Remolar et al., 2005 and discussed below].

323

324   **3. Methods**

325   **3.1 Hyperspectral Imaging Data**

326   *3.1.1 HyMap Data Analysis*

327

328   For remote observations of Rio Tinto we used aerial HyMap scenes that

329   covered the headwaters of the river, nearby mining activity, and urban areas. These

330   data were acquired by Integrated Spectronics on Aug 14, 2004 and are the same as

331   the fully processed and analyzed data used by Roach et al. [2006]. The reader is

332   directed to that publication for a detailed description of how these data were

333   calibrated, atmospherically corrected, and processed. Briefly, HyMap is an aerial,

334   hyperspectral system with 126 channels covering a wavelength range of 0.45 to 2.5

335   μm at a spatial resolution of ~8m per pixel. Spectra from the processed images were

336   examined for individual pixels as well as spectral averages from multiple pixels that

337   correspond to larger regions of geologic or spectral interest, called regions of

338   interest (ROIs). Wavelengths from ~1.3 - 1.45 μm and ~1.8 - 2 μm were excluded

339   due to atmospheric absorptions. A principal component analysis (PCA) was carried

340   out for the data to reduce spectral variance and to highlight regions with similar

341   spectral properties (Figure 3). PCA is a purely mathematical procedure and does not

342   rely on a user's *a priori* knowledge of variability in a region; thus, it can be difficult

343   to attribute different features observed in PCA images to unique differences in

344   mineralogy. However, as a purely qualitative tool we found this method reliable for

345   highlighting regions in the HyMap scenes whose spectra exhibited the doublet

346   absorption feature (e.g., Figure 3).

347

348   *3.1.2 CRISM Data Analysis*

349

350   CRISM is a hyperspectral imaging system on NASA's Mars Reconnaissance

351   Orbiter that consists of several spectrometers. The "L" spectrometer covers near-

352   infrared wavelengths from 1.0 to 3.9 μm using 431 channels, has a spectral

353   resolution of ~6.55nm per channel, and a maximum spatial resolution of ~15-19 m

354   per pixel [Murchie et al., 2007]. The highest spatial-spectral resolution images are

355   Full Resolution Targeted (FRT) observations, and for this study we analyzed three of

356   these images in detail from the western Valles Marineris region near Melas and Ius

357   Chasma (see Figure 4, Figure 9). A full description of CRISM image processing

358   methods is provided in the supplemental material.

359

360   The variability in the doublet absorption feature was studied in detail by

361   handpicking spectra from geologic units and ROIs that exhibited these spectral

362   features. The resulting spectra commonly represent 3x3 or 5x5 pixel averages.

363   Each spectrum was fit with an upper convex hull to define the spectral continuum

364   over the ~2.1 to 2.35 μm wavelength range. The original spectra were then divided

365   by these continuum fits to produce continuum-removed spectra. This step isolates

366   the wavelength region where the doublet occurs and is necessary to compare band

367   depths between spectra [Clark and Roush, 1984]. Band depth is defined as $1-[R_b(\lambda$

368     $)/R_c(\lambda)]$, where R_b represents the observed reflectance value at wavelength λ and

369   R_c represents the calculated reflectance of the spectral continuum fit at the same

370   wavelength. Band depth maps were created for each CRISM image to provide a more

371   in-depth analysis of the spatial distribution of the spectral doublet feature.

372

373   Gaussian curves were also fit to the continuum-removed doublet absorptions

374   and the resulting Gaussian amplitudes and center positions were mapped for each

375   CRISM image. Gaussian modeling of absorptions is commonly used for remote

376   sensing data to assess band strength in the presence of noise or to remove the

377   influence of adjacent or partially overlapping absorption features on the absorption

378   of interest [Clark and Roush, 1984; Sunshine and Pieters, 1993]. Noise in the CRISM

379   images, for instance, may introduce apparent changes in band position/strength if

380   these calculations are based on the observed absolute reflectance values on a pixel-

381   by-pixel basis. This can introduce uncertainties in the band depth maps, which we

382   attempt to mitigate by examining the amplitudes and positions of Gaussian fits.

383

384   To determine the background noise in an image prior to Gaussian fitting, a

385   histogram of the standard deviations within each image was examined for a flat,

386   absorption-free portion of the spectrum (1.70-1.85 μm), an example of which is

387   presented in Figure 4. Here it is clear that the standard deviations in the ratio

388   spectra are predominantly <0.005, thus any absorption feature (band depth) in the

389   ratio spectra that is larger than this value is above the typical level of 'noise' in the

390   CRISM image. Two CRISM ratio spectra exhibiting the doublet feature and their

391   corresponding Gaussian fits are also presented in Figure 4, where it is clear that the

392   doublet absorptions are much stronger than the typical channel-to-channel

393   variation in reflectance. Pixels that exceed the 0.005 threshold are fit with two

394   Gaussian curves, one for each absorption in the doublet (see example in Figure 4).

395

396   **3.2 Field Measurements**

397   Fieldwork was conducted at multiple locations in the vicinity of Rio Tinto,

398   Spain in early May of 2014. Rock and/or soil specimens were collected and field

399   spectra were acquired at each of five primary sites (Table 1). These locations

400   included the modern streambed environment and two successively older terraces

401   that have been affected to different degrees by diagenetic processes (Figure 2).

402   Previous studies have shown that the materials at these sites exhibit different

403   mineral assemblages [Fernández-Remolar et al., 2005; Fernández-Remolar and

404   Knoll, 2008], allowing us to examine whether spectral reflectance properties can be

405   linked to post-depositional processes in these types of environments.

406

407   Samples collected were collected from the Rio Tinto source region (Anabel's

408   Garden, Richi Spring, and Source Spring sites), a series of small streams with

409   actively forming efflorescent and crust-forming precipitates (e.g. copiapite, jarosite,

410   gypsum). A number of samples were also collected from an actively mined terrace

411   directly above Anabel's Garden that showed evidence for the spectral doublet

412   absorption in the airborne HyMap data. Another field site, Berrocal, is also located

413   directly on the Rio Tinto approximately 20 km downriver from the mining

414   operations. At this location, there is a mix of detrital sediment and authigenic

415   precipitates. We also examined older deposits at Barranco de los Locos, a site that is

416   part of the Holocene-aged lower terrace in which the lower unit is a ferruginous

417   conglomerate and is overlain by sandstone [Fernández-Remolar et al., 2005].

418   Finally, for comparison to the modern environment we examined an older (early

419   Quaternary) terrace exposed at Alto de la Mesa. Detailed descriptions of these sites,

420   their ages, and local geology can be found in previous publications [e.g., Fernández-

421   Remolar et al., 2005; Fernández-Remolar and Knoll, 2008; and references therein].

422

423   A portable VIS-NIR spectrometer (ASD FieldSpec 3®) was used to acquire

424   reflectance spectra *in situ* from 0.35 to 2.5 μm. Reflectance spectra were acquired

425   for a variety of materials passively (relying on ambient sunlight) and/or actively

426   (relying on a contact probe with internal illumination). All measurements were

427   made using a Spectralon® panel as the reflectance standard. Passive measurements

428   that rely on solar illumination and reflectance are more directly analogous to

429   airborne data such as HyMap. A more detailed description of the ASD measurements

430   is provided in the supplemental material.

431

432   Rock and sediment samples were collected to capture the spectral diversity

433   of deposits at each location and were based in part on interesting absorption

434   features observed in the HyMap and field reflectance spectra (see Table 1 for full

435   list). To the extent possible, samples were collected at the different sites to be

436   representative of the mineralogy expected at HyMap and CRISM spatial scales (e.g.,

437   the dominant mineral assemblages at scales of ~8 - 18 m/pixel, respectively),

438   focusing on regions whose spectra exhibited evidence for compositional diversity.

439   Of specific interest were regions with spectral or field-based evidence for Fe-oxides,

440   Fe-sulfates, and clay minerals. A number of locations contained materials whose

441   reflectance spectra exhibited the doublet absorption feature described above, and a

442   variety of these materials were collected for detailed laboratory characterization.

443   Though many other samples and spectra were collected during the field campaign,

444   the samples, field measurements, and HyMap data whose spectra exhibit these

445   distinct doublet absorptions were chosen as the focus for the present study. A more

446   complete treatment of how field-based spectral observations and diversity at Rio

447   Tinto relate to aerial and orbital-scale observations is presented in Roach et al.

448   [2006].

449

450   **3.3 Laboratory Measurements**

451   *3.3.1 Sample Preparation*

452   All laboratory analyses were conducted in the Department of Earth,

453   Environmental and Planetary Sciences at Brown University. A number of small chips

454   (~2.5 cm) were removed from each hand sample and a second portion of each was

455   ground by hand in an agate mortar and pestle. The resulting powders were ground

456   such that the material could pass through a <45 μm mesh sieve. Grinding and

457   sieving serves the dual purpose of homogenizing the sample and reducing particle

458   size-dependent absorption/scattering processes. Where possible, separate powders

459   were prepared for different portions of a single sample to assess heterogeneity (e.g.

460   rock varnish, dark or light components, areas with different degrees of weathering)

461   and for comparison to the whole rock powders. Some hydrated mineral phases are

462   expected to be unstable even over short time frames, and these are not included in

463   our dataset.

464

465   *3.3.2 Reflectance Measurements*

466

467   Reflectance spectra of the hand samples, chips, and powders were measured

468   in the laboratory using the same ASD FieldSpec 3 instrument over a wavelength

469   range of 0.35 to 2.5 μm. The measurement spot size was adjusted to encompass the

470   entire sample in order to provide a better assessment of the bulk spectral properties

471   of each hand, chip, and powder sample rather than averaging spectra of individual

472   components. We note that the chips and powder samples were placed in ~10 mm

473   diameter sample holders for measurement, thus the measurement spot size for

474   these samples is equivalent.

475

476   All of the rock powders sieved to <45 μm were also measured with a Nicolet

477   iS50 FTIR from 1.75 – 25 μm. The FTIR was equipped with a Praying Mantis diffuse

478   reflectance attachment from Harrick Scientific and diffuse gold from Labsphere was

479   used as a reflectance standard. These measurements used a KBr beamsplitter and

480   DTGS detector, and each final spectrum was an average of 50 scans. Absolute

481   reflectance values from the FTIR are highly dependent on any slight differences in

482   height between the sample and gold standard, thus all FTIR spectra were scaled to

483   match the ASD values at 1.7μm. These spliced spectra provide full VIS-NIR-mid-IR

484   wavelength coverage, and because all samples were measured under identical

485   conditions, the observed relative differences between samples are reliable.

486

487   All reflectance spectra (field and lab) were processed using the same

488   methods, and continuum-removed spectra and band depths were calculated using

489   the same procedures as described above for the CRISM data (i.e., an upper convex

490   hull method was used to define the continuum slope). We analyzed the continuum-

491   removed spectra using Matlab to find the local minima (which is equivalent to the

492   maximum band depth) within the ~2.1 – 2.35 μm wavelength region. If the

493   continuum-removed spectrum is determined to exhibit absorptions near ~2.2 μm

494   and ~2.26 μm, then this so-called doublet feature is further analyzed to determine

495   the total width, center position, and depth of the individual absorptions.

496

497   *3.2.3 X-ray Diffraction Measurements*

498

499   The <45μm sieved powders were measured with a Bruker D2 Phaser XRD

500   system (see supplemental material for details) to determine qualitative and

501   quantitative mineralogy. Samples whose corresponding reflectance spectra

502   exhibited the 2.2 μm doublet (n = 8) were studied in detail, as were a subset of

503   samples from multiple locations whose spectra did not exhibit the doublet (n = 3) in

504   order to test our hypothesis that a distinct mineral assemblage gives rise to the

505   doublet feature (Table 2). Powder diffraction patterns were typically acquired over

506   a range of 2-90° 2θ, 0.02˚ step size, with a total integration time of up to ~12 hours

507   (6.5 s/step).

508

509   XRD patterns were analyzed with two programs, DIFFRAC.SUITE™ EVA for

510   full pattern phase identification and DIFFRAC.SUITE™ TOPAS for quantitative

511   Rietveld refinement, where the latter is similar to the method described in Bish and

512   Howard (1988). An overview of the mineralogy at Rio Tinto is provided in

513   Fernández-Remolar et al. [2005], which we used as a guideline for choosing

514   reasonable starting components for the qualitative mineral assessment. Modal

515   mineralogy estimated from Rietveld refinement relied on the structural and

516   instrumental parameters to model the XRD patterns. Structure files describing the

517   crystallographic structure of relevant minerals used in the refinement are listed in

518   the supplementary table.

519

520   These mineral structures were added and removed from the model

521   iteratively until a reasonable fit to the observed pattern was obtained. TOPAS

522   automatically normalizes the model results such that mineral abundances will

523   always add to 100%. The quality of the refinement is determined by the weighted

524   profile R-factor (R_{wp}), which considers the root mean square error (RMSE) for each

525   scaled intensity value (peak and background). Although a smaller R_{wp} generally

526   indicates a better model, it is possible to over fit the data with this method and

527   discretion is used to ensure the resulting model is geologically realistic. We also

528   calculated the areas for the muscovite 001 (~9° 2θ) and jarosite 101 (~15° 2θ)

529   peaks. Though this method does not provide quantitative estimates like the Rietveld

530   method, it does provide an independent estimate of how the relative abundances of

531   the two minerals vary between samples without the uncertainties associated with

532   modeling the full XRD pattern.

533

534   **4. Results**

535   **4.1 Overview of Rio Tinto Field Observations**

536   Previous work has shown that mineralogical and spectral differences exist

537   between the old and young terraces [Fernández-Remolar et al., 2005; Sobron et al.,

538   2014], and we observe congruous spectral differences in our samples from these

539   locations. Field spectra of samples from the source region exhibit absorptions

540   consistent with the presence of gypsum, jarosite, and copiapite (Figure 5). Hydrated

541   iron-bearing phases are also common in these field spectra, including absorptions

542   consistent with the presence of schwertmannite and copiapite, which are identified

543   in spectra from the Richi Spring and Source Spring locations. The field spectra from

544   Berrocal (not shown) have very similar identifying absorptions that are typical of

545   the precipitates, phyllosilicates and iron hydroxides found in the source region

546   spectra. Spectra exhibiting the doublet absorption are found in sand bar sediments

547   from Berrocal, representing rocks/sediments that have not been influenced by

548   mining activities.

549

550   Most of the Fe- and Ca-sulfate precipitates are absent at the young terrace

551   site, Barranco de los Locos. Jarosite, Al-phyllosilicate (muscovite/illite), and goethite

552   are the primary minerals identified in our field spectra at this location. VIS-NIR

553   spectra from the old terrace site, Alto de la Mesa, exhibit the lowest mineral

554   diversity and are dominated by iron oxides. Most spectra from Alto de la Mesa are

555   consistent with the presence of goethite, though some indicate the presence of

556   kaolinite or chlorite. Sulfate absorptions are not apparent in spectra of materials

557   from the old terrace, and the doublet feature is also not observed in these spectra.

558   However, spectra for a number of samples that were taken from a mine road terrace

559   above Anabel's garden display the doublet absorption. Other samples from this site

560   are spectrally consistent with goethite and hematite. Finally, samples from some of

561   the mining terraces are spectrally consistent with chlorite, kaolinite, and muscovite,

562   likely reflecting country rock components.

563

564   **4.2 Laboratory Measurements**

565   *4.2.1 X-ray Diffraction*

566

567   Based on an initial qualitative assessment of the XRD patterns and observed

568   spectral diversity, eleven samples were chosen for further quantitative Rietveld

569   refinement. Eight of the samples have spectra that exhibit the spectral doublet and

570   contain between 3 - 38% jarosite and 4 - 50% illite or muscovite (Table 2). The

571   other volumetrically important mineral in these samples is quartz, which does not

572   have absorptions at VIS-NIR wavelengths, so the samples are spectrally dominated

573   by Fe-sulfate and Al-bearing clay minerals. K-jarosite is a better fit in the Rietveld

574   refinement than either hydroniumjarosite or natrojarosite. Though the mineral

575   assemblage is largely the same, the relative proportion of jarosite and Al-clay is

576   quite variable between samples (Figure 6), and these values are presented in Table

577   2. Three samples that do not show evidence for the doublet feature in

578   corresponding reflectance spectra were also examined. The XRD patterns for these

579   samples are consistent with a mineral assemblage dominated by hematite, goethite,

580   kaolinite, chlorite and quartz, but no jarosite, in agreement with the findings of

581   Fernández-Remolar et al., [2005] for this locale (Table 2). One sample from the

582   young terrace, Barranco de los Locos sample RT23, is modeled to contain ~33%

583   jarosite and ~39% gypsum but no Al-clay (Table 2), and its reflectance spectrum is

584   dominated by gypsum at wavelengths >1.3 µm (Figure 5). In summary, the major

585   secondary phases in these samples are jarosite, illite or muscovite, and Fe-oxides

586   such as goethite and hematite. Although smectitic clays are an integral part of the

587   alteration mineral assemblages on Mars, the Rio Tinto samples examined for this

588   study show no clear evidence for the presence of smectitic clays.

589

590   *4.2.2 Reflectance Spectra*

591

592   As with the field spectra, the laboratory spectra indicate variations in

593   mineral assemblage with age. In samples from the modern streambeds (samples

594   from Anabel's Garden and Source Spring) gypsum is the primary mineral identified

595   in two samples (RT18, RT23), with jarosite also being present in RT23 (see Figure

596   5). Other samples from these sites have spectra with strong OH and H_2O bands at

597   ~1.4 and ~1.9 µm as well as absorptions consistent with copiapite, schwertmannite,

598   or possibly monohydrated sulfates (Figure 5). These hydrated samples were not

599   measured with XRD because these minerals change hydration states readily under

600   laboratory conditions, so these spectral mineral identifications cannot be confirmed.

601   However, other XRD studies of Rio Tinto samples have found evidence for a variety

602   of sulfates, including epsomite, copiapite, and coquimbite [Fernández-Remolar et al.,

603   2005], and it is likely that a range of hydrated sulfates are also present in our

604   samples.

605

606   The spectral shapes of samples from the young terrace are distinct from

607 those of Anabel's Garden and Source Spring, with the former having weaker

608 hydration absorptions and a strong spectral slope near 1 μm. In fact, the major

609 difference in spectra of all the young terrace samples lie in the region between 2.2

610 and 2.3 μm; spectra of some samples show a doublet in this region whereas others

611 have only an ~2.21 or 2.27 μm absorption. Samples collected from the old terrace

612 deposit are spectrally consistent with clays such as kaolinite and chlorite as well as

613 Fe-oxides such as hematite (Figure 5). Gossan samples all show spectral evidence of

614 goethite. As with the field spectra, lab measurements of the older samples typically

615 lack spectral evidence for sulfates and are instead indicative of Fe-oxides and/or

616 phyllosilicates. Samples from the mining terrace have spectra that exhibit the

617 spectral doublet or that are representative of the same types of minerals discussed

618 for the other sites, including chlorite and Fe-oxides (goethite and hematite).

619 However, given that the specific geologic context of these samples is unknown,

620 especially compared to the well-defined mineralogical and age progression of the

621 river terraces, it is difficult to comment on the processes that have affected this

622 group of samples.

623

624   To summarize thus far, laboratory spectra with the doublet absorption

625 correspond to samples collected from the modern stream sites (Anabel's Garden,

626 Source Spring), the young terrace (Barranco de los Locos), and from a mining

627 terrace site near Anabel's Garden (Table 2). There are many minerals that have

628 spectral features near 2.26 μm, but we attribute the 2.26 μm feature in the doublet

629   to jarosite because of the combined presence of absorptions at wavelength positions

630   that are attributed to jarosite (1.48, 1.86, 1.9, 2.26 μm), as well as evidence from

631   XRD mineralogical analysis. The doublet feature is conspicuously absent in spectra

632   of samples collected at the old terrace, all of which lack jarosite. Reflectance spectra

633   of the <45 μm powders of samples exhibiting the doublet show strong, broad

634   electronic transition absorptions at wavelengths of ~1 μm due to the presence of

635   iron (Figure 6). There are also narrower vibrational absorption features at 1.4 and

636   1.48 μm due to OH, though the 1.48 μm feature is weak or absent in samples that

637   show a very strong 2.21 μm short wavelength band in the doublet feature. Likewise,

638   a broader absorption at ~1.9-1.95 μm due to OH/H_2O and a narrower absorption at

639   1.86 μm from OH/H_2O are also weaker in samples with a stronger ~2.21 μm

640   feature.. In contrast, the ~2.21 μm absorption in the doublet feature is related to the

641   presence of Al-phyllosilicates (illite or muscovite). A vibrational absorption near

642   2.35 μm is present in some samples and is also consistent with the presence of Al-

643   OH in illite or muscovite.

644

645   Spectra of rock chips and hand samples were also acquired and, in most

646   cases, the samples whose powder spectra exhibited the doublet feature also exhibit

647   the feature for these larger physical forms (see example for sample RT19 in Figure

648   7). However, sample RT10 is an exception in that a spectrum of the orange-colored

649   varnished face of the hand sample shows the doublet feature whereas the

650   unvarnished side of the hand sample, a chip, and the powder spectra are dominated

651   by the 2.21 μm feature (Figure 7). This indicates the varnish may be enriched in

652   jarosite, and although such coatings or varnishes may be only several micrometers

653   thick, they may contribute significantly to aerial and orbital spectral observations.

654

655   Only the bulk powder versions of the samples were measured using both

656   reflectance spectroscopy and XRD; thus, we compare only the powder spectra

657   directly with the mineralogy determined by XRD. There is a strong correlation

658   between the strength of the longer wavelength absorption in the doublet feature

659   and the abundance of jarosite for the samples examined here (Figure 8). There is

660   also a strong relationship between the relative band strengths and the relative

661   amounts of jarosite and Al-clay in the samples, as determined using either the

662   Rietveld modal estimates or the XRD peak area. The relationship between Al-clay

663   and the strength of the shorter wavelength absorption has a lower R^2 value than in

664   the other plots, but we suggest this is due to the size of the dataset, where a

665   relatively small amount of scatter (in this case one data point with anomalously high

666   estimated Al-clay wt.%) has a strong control on the fit. These observations indicate

667   that the doublet feature observed in spectra of some samples from Rio Tinto is

668   related to the mixing of Al-phyllosilicate (illite or muscovite) with jarosite, and that

669   the strengths of the absorptions within the doublet feature are directly related to

670   the relative proportion of these phases.

671

672   **4.3 HyMap and CRISM Observations**

673   *4.3.1 HyMap Results*

674

675   The HyMap PCA false-color map presented in Figure 3 highlights pixels

676   whose spectra exhibit the doublet feature in dark red. Absorption maxima

677   (reflectance minima) for these pixels occur at ~2.20-2.22 and 2.26-2.28, a range that

678   is broader than observed in Mars CRISM data and that could be a result of

679   differences in spectral resolution, since HyMap only has 6 bands in this wavelength

680   region compared to CRISM's 13 bands. The doublet feature is evident in HyMap

681   spectra corresponding to the Anabel's Garden location, where it is possible to track

682   changes in the relative strength of the absorptions across a ~500 m transect in the

683   HyMap image (Figure 3). The feature is also present in numerous pixels

684   corresponding to mining terraces, although it was not possible to independently

685   examine most of these locations during the field study. Bedrock, detritus, and soil at

686   the young, intermediate, and old terrace sites discussed above are not always

687   apparent in the HyMap data due to the presence of vegetation. However, chlorite,

688   kaolinite, gypsum, and Al-clay are identifiable in the HyMap spectra, and Roach et al.

689   [2006] provide a thorough analysis of iron oxides and hydrated or hydroxylated

690   iron-sulfates in these airborne data. In this study we have only relied on the HyMap

691   data to provide an airborne comparison (at lower spatial and spectral resolution) of

692   the doublet-bearing materials with the spectra acquired in the lab and *in situ* using

693   the ASD FieldSpec3. In this context, the HyMap data confirm that spectra of certain

694   surface materials exhibit the doublet feature even at a meters-per-pixel spatial scale

695   and lower spectral resolution, consistent with the higher spatial and spectral

696   resolution field and laboratory data.

697

698   *4.3.2 CRISM Results*

699

700   The spectral doublet feature is evident in a number of CRISM images in the

701   Valles Marineris, with particularly good examples in Melas and Ius Chasma [e.g.

702   Roach et al., 2010, Weitz et al., 2014]. Our Gaussian fit analysis of three of these

703   CRISM images show that the absorption band centers and relative strengths

704   (Gaussian amplitudes) associated with the doublet materials are only moderately

705   variable (Figure 9). The centers of the Gaussian fits for the three CRISM images and

706   the HyMap image are listed in Table 3. The typical 2σ deviation on the band

707   positions in the CRISM images is ~0.015 μm and the band centers fall near 2.2060

708   and 2.2682 μm on average. However, the wavelength position varies across the

709   spatial dimension of the CRISM detector (spectral smile) by ~0.010 μm, which may

710   explain much of the width of the histograms in Figure 9. To examine this effect we

711   analyzed a 50 x 50 pixel region restricted to the center of each image where the

712   spectral smile is minimal. Histograms for these subsets reveal a decrease in

713   standard deviation as well as a shift in mean band center in all three cases (Table 3,

714   Figure 4). The difference in band centers between the full image and the central

715   subset is statistically significant ($p < 0.05$) in every case.

716

717   Therefore, we conclude that the band centers of the doublet spectral feature

718   are relatively constant and occur at wavelengths of ~2.21 and ~2.265-2.270 μm. It

719   should be noted that Weitz et al. [2014] identified another spectral doublet

720   occurrence with a long wavelength absorption closer to ~2.28 μm, and the inclusion

721   of pixels with this feature in our analysis would create additional spread in the

722   histograms in Figure 9c. Given that we did not analyze each pixel in each image

723   individually, it is possible that this longer wavelength doublet is present, but it is

724   certainly not a dominant spectral signature, which is evident in the histograms and

725   investigation of spectra from individual pixels and ROIs.

726

727   While the wavelength positions of the two absorptions appear to be fixed,

728   their relative strengths are variable and are not directly correlated (Figure 9d).

729   Though this result is qualitatively similar to what is observed in field, lab and

730   HyMap spectra of materials from Rio Tinto, the range in relative amplitudes of the

731   two absorptions is typically much smaller in the CRISM data than for the terrestrial

732   examples. That is, spectra of some materials from Rio Tinto are clearly dominated

733   by the ~2.21 or the ~2.27 μm feature, with the other feature being very weak or

734   absent. In contrast, nearly all CRISM spectra for the regions examined here exhibit

735   both features and in many instances both features are of equal strength and, while

736   variability does exist, it is less intense than the variability in strengths observed in

737   the Rio Tinto spectra.

738

739   The relative band strengths, which is the Gaussian amplitude of the 2.21 μm

740   absorption divided by the amplitude of the 2.27 μm absorption, for the three CRISM

741   images is 1.1925±1.47 (2σ), 1.2714±1.35 (2σ), and 1.2207±1.28 (2σ). These

742   averages suggest that the band strength of the shorter wavelength absorption is

743   often slightly stronger than the longer wavelength absorption. However, the

744   standard deviation of the distribution is large enough that it is clear the two

745   absorptions do not co-vary. That is, the two absorptions that comprise the doublet

746   feature in CRISM spectra are independent of one another and thus represent two or

747   more distinct phases. Both tails of the distributions in Figure 9d are affected by

748   "bad" pixel values (typically a spike in the value for a single CRISM channel in one

749   column of the image that will influence the Gaussian fits). This is particularly

750   obvious as a bulge in the distribution as the Band 1/Band 2 amplitude ratio

751   approaches 0 (due to Band 1 amplitudes approaching 0) as well as by the long tail as

752   the Band 2 amplitude approaches 0, starting at a band amplitude ratio of ~3.

753   However, other than the extreme tails of the distributions (which represent a

754   relatively small number of pixels), these pixels play a minimal role in the overall

755   distributions of the band amplitude ratios.

756

757   **4.4 A Case Study: Doublet-Bearing Materials in Ius Chasma, Mars**

758

759   This study is focused on the spectral characteristics of materials found on

760   Mars and how they relate to those in Rio Tinto as seen in field, airborne, and lab

761   data, with the goal of assessing whether or not the latter may be appropriate

762   mineralogical analogs. However, to fully understand the processes and

763   environmental conditions associated with the deposits on Mars, and whether or not

764   Rio Tinto is an appropriate process analog, it will be necessary to conduct detailed

765   mapping studies that place the martian examples in their proper geologic context.

766   We conducted a small-scale examination of MRO HiRISE and CTX images of the

767   doublet-bearing materials in Valles Marineris to get a sense of the stratigraphic

768   position of these deposits with respect to surrounding strata.

769

770   As discussed by Roach et al. [2010], some occurrences of the materials with

771   the doublet absorption are in proximity to Fe/Mg clay-bearing strata. However, in

772   many cases the contacts between units are obscured and bedding is not apparent,

773   making it difficult to determine the relative stratigraphic position of these units.

774   Despite these complications, it is clear that the doublet absorptions are commonly

775   associated with light-toned units that drape pre-existing topography and span a

776   range in elevation (e.g., Figure 10a) or as deposits within the topographically lower

777   portions of the chasma (e.g., Figure 10b). In some locations the doublet unit

778   surrounds the clay-bearing units, whereas in others the clay-bearing unit is located

779   higher up the canyon wall. The doublet material also occurs as matrix in

780   megabreccia deposits [Roach et al., 2010], an example of which can be seen in

781   CRISM image FRT0000A396 in Figure 9. We now discuss a case study for one region

782   in Ius Chasma where several doublet-bearing units are in proximity to Mg/Fe clay-

783   bearing strata, focusing on the relative stratigraphic position of these units in order

784   to assess the relationship between the observed mineral assemblages in a more

785   detailed geologic context.

786

787   The relative strength of absorptions in the doublet feature were mapped for

788   several CRISM observations in Ius Chasma and overlain on HiRISE and CTX images

789   (Figure 11). This map reveals both the full extent of the doublet-bearing units and

790   allows for further discrimination of spectral properties within and between the

791   different units. Each colored pixel meets the criteria of having band depth > 0.005 at

792   both 2.205 and 2.269 μm. Where the ratio of band depths (BD 2.205/2.269 μm) is

793   small, we interpret the unit to be enriched in the ~2.27 μm phase, and a higher ratio

794   represents the opposite, in a strictly relative sense. In some locations (Figure 11c)

795   there is a full transition between these cases within a single unit. In this example,

796   the unit is heavily brecciated and lacks clear stratification. This example fits within

797   a larger regional trend where the doublet-bearing units with the strongest ~2.27

798   μm absorption are in the south, and seemingly higher up the walls of the chasm,

799   which then transitions to a topographically lower region where the doublet has an

800   absorption with two bands of equal strength, and finally to the north where the

801   ~2.21 μm absorption becomes stronger in the floor units (see the red-to-green-to-

802   blue northerly progression in Figure 11b). In this example it is clear that the

803   doublet-bearing unit is quite heterogeneous with regard to the strength of the two

804   absorptions, suggesting the relative abundances of the phases responsible for these

805   absorptions are also highly variable within this single geologic unit.

806

807   A second example reveals changes in composition that are consistent with

808   geomorphologic changes and that conform to geologic contacts. Three doublet-

809   bearing units ("bright", "light", and "moderate"-toned) and a darker, stratified,

810   Mg/Fe clay-rich unit are shown in Figure 11d, with close-up HiRISE views of the

811   contacts between these units presented in Figure 12. The Mg/Fe clay unit has tilted

812   strata (dipping approximately north/northwest, see Figure 12b) and spectra for

813   these units do not meet the criteria for being "doublet bearing" (with the exception

814   of a few pixels that have high band ratios and therefore higher amounts of the ~2.21

815   μm component). These stratified Mg/Fe clay units are superposed by a light-toned

816   doublet-bearing unit. The significant difference in bedding geometry and the sharp

817   nature of the contact suggests there is an angular unconformity between these units,

818   with the clay strata predating the doublet-bearing unit (Figure 12b). This light-

819   toned doublet unit has a relative band strength ratio of ~1, meaning the absorptions

820   within the doublet are of equal strength (however, this does not necessarily imply

821   that there must be equal amounts of each component). Overlying this unit is a

822   second doublet-bearing unit that is moderate in tone but that exhibits similar

823   morphological characteristics as the light-toned unit (Figure 12c). At full HiRISE

824   resolution it is apparent that both the light and moderate-toned units are stratified.

825   The moderate-toned unit has a band strength ratio between 1.2 and 1.8, indicating

826   the shorter wavelength (~2.21 μm) absorption is stronger.

827

828   The third unit in this region corresponds to pixels with band ratios <0.9,

829   consistent with it being enriched in the longer wavelength (~2.27 μm) component

830   relative to the other doublet-bearing units in this location. This unit is the brightest

831   in grayscale HiRISE and CTX images and is overlain by the light-toned unit (Figure

832   12d). In this location there is no direct contact between the dark-toned Mg/Fe clay

833   strata and this bright unit, thus the relative stratigraphic order cannot be

834   determined. However, in nearby locations it appears that this bright-toned unit that

835   is characterized by a stronger ~2.27 μm band is also stratigraphically above the

836 Mg/Fe clay-bearing unit, though these individual outcrops are too small to identify

837 compositionally with CRISM. Therefore, the apparent increasing stratigraphic order

838 is: Mg/Fe clay strata – (angular unconformity) – bright unit – light unit – moderate

839 unit. The associated mineralogy above the unconformity appears to decrease in the

840 longer wavelength ($\sim$2.27 µm) component and increase in the shorter wavelength

841 ($\sim$2.21 µm) component upsection, at least in a relative sense.

842

843   Together, these two examples indicate that the relationships between the

844 minerals responsible for the doublet feature and the local stratigraphy are diverse.

845 In the first example there appears to be spectral variation, and thus relative changes

846 in mineral abundance, within a single geologic unit. In the second case the dominant

847 spectral variations appear to conform to stratigraphic boundaries, indicating

848 differences in relative mineral abundance as a function of geologic unit and

849 stratigraphic position.

850

851

852 **5. Discussion**

853 *5.1 Mineralogy*

854

855   The CRISM spectral doublet feature is similar to features observed in

856 airborne, field, and laboratory spectra of materials in and around Rio Tinto, Spain.

857 As discussed above, XRD analysis of select Rio Tinto samples demonstrates that this

858 spectral doublet arises from a mixture of Al-bearing phyllosilicates and jarosite. By

859   analogy, CRISM spectra exhibiting the doublet feature may also arise from a mixture

860   of Al-phyllosilicates and jarosite, one of the possibilities discussed by Roach et al.

861   [2010] and Weitz et al. [2014]. This interpretation is supported because (1) the two

862   absorptions that comprise the doublet feature vary independently, suggesting at

863   least two phases are present, (2) the absorption features within the martian doublet

864   examples occur at the same wavelength positions as observed in the Rio Tinto

865   spectra and are consistent with Al-OH and Fe-OH vibrations, and (3) the doublet-

866   bearing material occurs on Mars in the vicinity of other phyllosilicate and/or

867   jarosite-bearing deposits. Therefore, we conclude that Al-phyllosilicate-jarosite

868   mixtures in the Rio Tinto may serve as *spectral* analogs for the doublet materials

869   found in the Valles Marineris and elsewhere on Mars. However, whether or not the

870   Rio Tinto deposits may also serve as *process* analogs warrants further study, as

871   discussed below.

872

873   Other suggestions for the doublet feature have included opaline silica and

874   clay, mixtures of sulfates (e.g. gypsum and jarosite), and poorly crystalline $Fe-SiO_4$-

875   bearing phases. Reflectance spectra of opaline silica do exhibit a broad absorption

876   feature from 2.2-2.26 μm [Milliken et al., 2008], but it has been noted that this

877   feature is typically too broad to match the doublet even when mixed with Fe-rich

878   clay such as nontronite [Weitz et al., 2014]. One of our Rio Tinto hand samples,

879   RT23, provides a natural example of an intimate mixture of jarosite and gypsum in

880   which there are similar proportions of both phases and no phyllosilicates (Figure 5).

881   The reflectance spectrum of this sample is clearly dominated by the H_2O absorptions

882   characteristic of gypsum and an absorption near 2.2-2.3 μm that is wider than

883   observed for the typical doublet feature. In addition, although gypsum exhibits very

884   narrow absorption features near ~2.22 and ~2.27 μm, these are rather weak and

885   they are superposed on the much broader and stronger feature that spans the

886   ~2.08-2.3 μm region (see gypsum spectrum in Figure 1). By contrast, the

887   absorptions in the doublet feature do not appear to be superposed on any broader

888   feature and each appears to be much stronger and more clearly defined than the

889   narrow features observed at similar wavelengths in gypsum. In summary, it does

890   not seem possible to recreate the shape of the doublet feature through a

891   combination of only gypsum and jarosite, thus we consider the doublet feature to be

892   most consistent with a mixture of an Al-phyllosilicate and jarosite.

893

894   In our Rio Tinto samples the Al-phyllosilicate is dominated by illite or

895   muscovite and is likely to be detrital, sourced from the surrounding country rock. In

896   contrast, the jarosite, which in some samples occurs as a coating, is authigenic and a

897   natural product of the Fe- and S-rich, oxidizing, acidic conditions that characterize

898   the Rio Tinto system. The decrease in jarosite with progression in age suggests it is

899   not stable over geologic time in the continued presence of water, particularly for

900   circum-neutral and higher pH fluids. Indeed, we observe the doublet feature only in

901   spectra that contain jarosite, which are primarily associated with the youngest

902   deposits such as those at Anabel's Garden and at the Source Spring. It is notable that

903   in our Rio Tinto samples the spectral doublet feature can be directly attributed to

904   relatively well-crystalline phases as there is no clear spectral or XRD evidence for

905   hydroxylated poorly crystalline phases that may result from the acidic leaching of

906   clay minerals. This is not to say that such processes do not occur in these locations,

907   but rather to note that the presence of acid-leached clays or hydrated poorly

908   crystalline precipitates are not required to explain the presence of the spectral

909   doublet feature in the samples examined here.

910

911   The same may not be true of the doublet-bearing materials on Mars. There,

912   acidic leaching of basalt and/or pre-existing smectitic clays may be an important

913   process for forming alteration minerals, including some sulfates such as jarosite

914   [e.g., Tosca et al., 2004; Golden et al., 2005]. As noted above, acid-leaching of clays

915   has also been invoked to explain the presence of the spectral doublet feature on

916   Mars [Tosca et al., 2008b; Roach et al., 2010; Noe Dobrea et al., 2011; Weitz et al.,

917   2014], and the occurrence of jarosite in some locations is indicative of low-pH

918   conditions, at least at a local scale. It is possible to make a poorly crystalline Fe-SiO_4-

919   bearing material through the acid leaching of nontronite, and reflectance spectra of

920   such products can exhibit absorptions with band centers similar to those observed

921   in the doublet feature [Madejova et al., 2009; Roach et al., 2010]. In this scenario, the

922   relative strengths of the absorptions may vary based on the degree of acid

923   alteration. However, spectra of residues from the acid leaching of nontronite may be

924   more consistent with Si-rich, opaline-like materials, and in these cases the full width

925   of the resulting doublet feature is slightly wider than is observed in the martian

926   examples [Tosca et al., 2008b; Altheide et al., 2010].

927

928   As a different example, reflectance spectra of Fe/Mg smectite-rich altered

929   basalts from Mauna Kea, Hawaii that have undergone acid leaching exhibit a doublet

930   feature that is thought to arise from the presence of jarosite and hallyosite [Graff et

931   al., 2012]. In this instance the spectral doublet feature is the result of two distinct

932   (presumably authigenic) mineral phases likely produced by

933   dissolution/transformation of pre-existing phases and not associated with a poorly-

934   crystalline leached clay residue. The spectral characteristics of halloysite-jarosite

935   mixtures, as presented in Graff et al. [2012], are more consistent with the doublet

936   characteristics observed on Mars than are the spectral characteristics of a Si-rich

937   leached clay residue. Spectra of the latter tend to exhibit absorptions in the ~2.2-2.3

938   μm region that span a slightly broader wavelength range than the martian examples

939   and for which the individual absorptions are not as narrow or well-defined as the

940   martian examples. Halloysite and kaolinite are spectrally similar in the ~2.2-2.3 μm

941   region, thus halloysite-jarosite, kaolinite-jarosite, and montmorillonite/illite-

942   jarosite mixtures could all be consistent with the martian doublet materials.

943

944   Perhaps akin to the observations by Graff et al. [2012], laboratory

945   experiments by Tosca et al. [2008b] indicate that dissolution of basalt and addition

946   of sulfur could lead to fluids that form precipitates under oxidizing conditions

947   whose spectra also exhibit a doublet between 2.2 and 2.3 μm [see example spectrum

948   in Roach et al., 2010]. Though some of the precipitates generated during these

949   experiments were X-ray amorphous, others exhibited XRD patterns consistent with

950   neoformation of jarosite, Fe-oxides, and opaline silica [Tosca et al., 2008b]. VIS-NIR

951   reflectance spectra of these precipitates were also consistent with the presence of

952   opaline silica, minor jarosite, and an Al-OH bearing phase, though the mineralogical

953   host(s) of observed Al-OH bands at ~2.21 μm was not directly evident in the XRD

954   data and it/they may be below the XRD detection limit.

955

956

957   *5.2 Formation Processes: Detrital and Authigenic*

958

959   From a process point of view the distinction between the scenarios described

960   above may be somewhat semantic. The important point is simply the recognition

961   that dissolution and alteration of basaltic materials on Mars, including cases where

962   clay minerals may already be present, can lead to fluids capable of forming jarosite

963   and Al-rich phyllosilicates. However, co-occurrence in the martian deposits does not

964   necessarily imply that both jarosite and Al-phyllosilicates were formed at the same

965   time, under the same conditions, or even in the same region. Either mineral could be

966   detrital or authigenic in the doublet-bearing units, and detailed geologic context in

967   conjunction with an assessment of the full mineral assemblage is needed to assess

968   which scenario is most likely.

969

970   Given that halloysite, kaolinite, muscovite/illite, and montmorillonite all

971   exhibit an absorption feature at ~2.21 μm and that all have been identified on Mars

972   from CRISM data [Ehlmann et al., 2009], it may be difficult to unambiguously

973   determine which Al-bearing phyllosilicate is present in these purported mixtures

974 using VIS-NIR reflectance spectroscopy alone. There is evidence in some of the

975 martian spectra that the doublet feature may exhibit a shoulder on the short

976 wavelength side of the ~2.21 μm absorption, indicating a weak and narrow

977 absorption may be present in the ~2.15-2.21 μm region. If true, this could be more

978 consistent with the presence of kaolinite or halloysite as the Al-bearing

979 phyllosilicate as opposed to illite or muscovite or montmorillonite. The presence of

980 jarosite would indicate low-pH conditions (at least locally), and previous studies

981 have noted that kaolin minerals can be formed under acidic conditions [e.g., Fialips

982 et al., 2000]. On Mars, oxidation of fluids enriched in ferrous iron could lead to local

983 (and transient) acidification, which could promote jarosite formation if sulfides are

984 present or if sulfate is present in solution [e.g., Hurowitz et al., 2009, 2010].

985

986   The processes described above indicate the possibility that both the Al-

987 phyllosilicates and jarosite are authigenic and thus indicative of local aqueous

988 geochemical conditions. Though some Al-phyllosilicates can form under moderate

989 to low-pH conditions, particularly kaolinite, an alternative possibility is that the Al-

990 phyllosilicates in the martian doublet materials are detrital. In this scenario the

991 jarosite would be indicative of local aqueous conditions and the phyllosilicates

992 would reflect eolian or aqueous sediment transport processes. If true, the doublet-

993 bearing units in Valles Marineris may be similar to Rio Tinto in terms of mineralogy

994 *and* process, in which case the relative proportions of Al-phyllosilicate and jarosite

995 in a given deposit could reflect the relative contributions of sediment input and

996 mineral precipitation, respectively. Recent experimental work by Dixon et al. [2015]

997   demonstrated that jarosite dissolution is not strongly dependent on hydrologic

998   conditions and that 1 mm jarosite particles are unlikely to survive for more than 10^4

999   - 10^5 years even at low flow rates (<0.01 L hr^{-1}). Therefore, while it is possible that

1000   the jarosite on Mars may be detrital, this is unlikely to be the case for long-lived

1001   fluvial transport systems, similar to the lack of jarosite observed in the older

1002   deposits at Rio Tinto. That stated, because we cannot constrain the particle size of

1003   the jarosite we cannot rule out eolian transport for this component.

1004

1005   A detailed 'source to sink' and stratigraphic study of the geologic setting of

1006   each of the doublet bearing units on Mars is needed to help determine which ones

1007   may represent diagenetic/authigenic phases (do observed mineral boundaries cut

1008   across the stratigraphy?) versus those that may be detrital (do variations in

1009   mineralogy conform to stratigraphic boundaries?), which is beyond the scope of the

1010   current study. However, given the diversity in morphologic properties of the

1011   doublet-bearing units within Valles Marineris and the results of the case study

1012   described above, it is likely that multiple formation processes are responsible even

1013   though the spectral signatures are similar.

1014

1015   The massive brecciated deposit in Ius Chasma that shows a relative

1016   transition from more jarosite to more Al-phyllosilicate within a single geologic unit

1017   (first example in our case study, Figure 11c) could be evidence of *in situ* alteration.

1018   Similarly, the thin draping units such as the one shown in Figure 10a are difficult to

1019   explain by processes other than airfall deposition [e.g., Weitz et al., 2015], which

1020   would suggest a relatively fine grain size and thus make the original sediment more

1021   susceptible to chemical alteration if it has not been welded. In this case, the draping

1022   unit may be an airfall dust or volcanic ash deposit, either of which could contain

1023   sulfur, that was later altered by water, possibly in the form of thins films from

1024   melting snow or ice. Atmospheric sources of sulfur (e.g., from volcanic emissions)

1025   could also contribute to authigenic sulfate formation. Regardless of the source, local

1026   differences in iron and/or sulfur content of the original sediment would lead to

1027   different authigenic mineral assemblages, such as different amounts of Al-

1028   phyllosilicate and jarosite [Michalski et al., 2013].

1029

1030   The second example in our case study of Ius Chasma , where Mg/Fe clay-

1031   bearing strata are unconformably overlain by layers have differing amounts of

1032   inferred jarosite and Al-phyllosilicate (Figures 11-12), may be more consistent with

1033   changes in sediment flux and/or source region. The stratigraphic order of these

1034   units indicates the large Fe/Mg clay unit pre-dates deposition of the units with the

1035   doublet feature. Indeed, there is no clear genetic relationship between the Mg/Fe

1036   clay unit and the doublet units, suggesting the latter are inconsistent with *in situ*

1037   alteration or leaching of the former. One possible interpretation is that the different

1038   proportions of the Al-phyllosilicate component, which correspond to distinct

1039   stratigraphic units, represent changes in sediment flux and or source region,

1040   perhaps where an increase in Al-phyllosilicate corresponds to a more highly

1041   weathered source region. Unlike the other example we presented for this region, the

1042   relative strength of the ~2.27 μm jarosite absorption also appears to conform to

1043   stratigraphic boundaries. This may indicate that the jarosite is also detrital, but an

1044   authigenic origin is possible as well since pore fluid flow or chemistry may be

1045   stratigraphically controlled.

1046

1047   If this sequence in Ius Chasma does in fact represent different relative

1048   amounts of authigenic jarosite and detrital Al-phyllosilicate, then we are potentially

1049   observing an upsection transition from precipitate (jarosite) dominated lithologies

1050   to ones dominated by clastic input. Such stratigraphic changes in mineralogy could

1051   be formed in a variety of environments, and without modal abundances for these

1052   minerals it is difficult to narrow the possible interpretations. However, possibilities

1053   include decreasing either the abundance of jarosite cement (which may or may not

1054   correspond to a change in absolute Al-phyllosilicate content), the availability of

1055   water, and/or Fe or S availability. Alternatively, a change in redox conditions, pH, or

1056   an increase in detrital input through time could also influence the relative

1057   proportions of jarosite and Al-phyllosilicate. Regardless, the observation that there

1058   are deposits suggestive of both *in situ* alteration and a combination of detrital influx

1059   of clay and precipitation of sulfate shows that multiple aqueous processes were

1060   likely responsible for formation of the doublet-bearing materials.

1061

1062   One of the most intriguing features of the doublet-bearing rocks at Rio Tinto

1063   is that the associated mineral assemblage is not preserved through geologic time in

1064   a terrestrial environment. Influx of fresh meteoritic water removes sulfates,

1065   including jarosite, and results in a net increase in ferric oxides, predominantly

1066   goethite, through time [Elwood Madden et al., 2004; Golden et al., 2005]. The

1067   transition from young sulfate-rich streambed deposits to older ferric oxide-rich

1068   terraces takes place in less than a million years, which is in agreement with jarosite

1069   dissolution rates reported by Dixon et al. [2015]. That study also noted that jarosite

1070   dissolution rate is more likely to be controlled by mineral-surface reaction rates

1071   rather than hydrologic conditions. Assuming that the Valles Marineris deposits have

1072   been exposed on the surface since at least the Early Amazonian, the apparent

1073   persistence of jarosite indicates that interaction between the doublet materials and

1074   water (e.g., diagenetic overprinting) has been rather limited since the time of

1075   jarosite formation or deposition. Thus, while water is required for the formation of

1076   jarosite and phyllosilicates, and for some occurrences of the doublet materials water

1077   may have acted as a sediment transport agent, it is likely that post-deposition water-

1078   rock interaction has been significantly limited in these regions for hundreds of

1079   millions of years or longer.

1080

1081   In summary, it is important to keep in mind that the presence of a mineral or

1082   mineral assemblage in and of itself is not necessarily indicative of local aqueous

1083   geochemistry for a given outcrop or region. Mineral identifications, particularly

1084   those determined at spatial scales that are typical of orbital spectrometers (10s of

1085   meter per pixel or greater), must be placed in proper context to determine how they

1086   relate to geologic processes and environmental conditions. Specifically, it is critical

1087   to determine which minerals may be detrital versus authigenic (to the extent

1088   possible) and to assess the textural relationships between different mineral phases.

1089   Do sulfates and/or phyllosilicates occur as cementing agents, vein fill, or clasts? For

1090   minerals that are indicative of specific chemical conditions, such as jarosite, does the

1091   abundance and/or presence of the phases require those conditions to be persistent

1092   or might they represent short-lived exceptions to very different background

1093   conditions? As it stands, addressing such questions typically requires detailed small-

1094   scale observations that are only achievable by rovers or humans, thus caution

1095   should be exercised when interpreting orbital observations in terms of specific

1096   geologic processes, particularly at small spatial scales.

1097

1098   **6. Summary and Conclusions**

1099

1100   An enigmatic doublet feature in reflectance spectra has been observed

1101   alongside hydrated mineral deposits in a number of regions on Mars. Previous

1102   studies have proposed that this spectral signature could arise from mixtures of

1103   hydrated minerals with known absorptions between 2.2 and 2.3 μm, including

1104   jarosite, gypsum, silica, Fe/Mg smectite, and Al-phyllosilicates. Possible spectral and

1105   mineralogical analogs from Rio Tinto are analyzed with a combination of laboratory,

1106   field, and aerial reflectance spectra and XRD analysis of the mineralogy and reveal

1107   that the doublet arises in rocks containing both illite or muscovite and jarosite. The

1108   martian doublet materials are also consistent with a mixture of Al-phyllosilicate and

1109   jarosite because (1) the wavelength positions of the martian doublet absorptions

1110   are similar to those observed in Rio Tinto data collected at lab, field, and airborne

1111   spatial scales, (2) the wavelength positions and widths of individual absorptions are

1112   consistent with the presence of Al-OH and Fe-OH-bearing minerals, and (3) the

1113   strengths of the two absorptions in the doublet vary independently, implying the

1114   spectra represent a mixture of two or more components. Likely Al-phyllosilicates for

1115   the martian examples include montmorillonite, illite, and kaolinite/halloysite.

1116

1117   Two scenarios are proposed for the creation of these clay-sulfate

1118   assemblages on Mars in the context of a case study of deposits in Ius Chasma. In one

1119   example there are clear mineralogical changes (variations in relative proportions of

1120   jarosite and Al-phyllosilicate) within a single breccia unit. These deposits are

1121   consistent with *in situ* jarosite formation, possibly linked to diagenetic fluids. In a

1122   second example, observed changes in the relative proportions of the two minerals

1123   appear to follow stratigraphic boundaries, and in all cases the doublet-bearing units

1124   lie unconformably over Mg/Fe clay-bearing strata. A detrital origin for both phases

1125   cannot be ruled out in this case, but it is also plausible that the observed changes in

1126   mineralogy reflect changes in the relative contribution of precipitates (e.g., jarosite)

1127   versus detritus (e.g., Al-phyllosilicates) through time. Both detrital and authigenic

1128   origins are consistent for different doublet-bearing deposits in Ius Chasma, and the

1129   complexity of these deposits demonstrates the need for detailed mapping of each

1130   occurrence to decipher their likely geologic history. The results of such detailed

1131   mapping studies will ultimately provide the most insight into what these deposits

1132   record about aqueous activity, preservation potential, and water-rock-atmosphere

1133   interaction on Mars.

1134

References

Altheide, T.S., Chevrier, V.F., Noe Dobrea, E., 2010. Mineralogical characterization of acid weathered
         phyllosilicates with implications for secondary martian deposits. Geochimica et Cosmochimica
         Acta 74, 6232–6248. doi:10.1016/j.gca.2010.08.005
Arvidson, R.E., Ruff, S.W., Morris, R.V., Ming, D.W., Crumpler, L.S., Yen, A.S., Squyres, S.W., Sullivan,
         R.J., Bell, J.F., Cabrol, N.A., Clark, B.C., Farrand, W.H., Gellert, R., Greenberger, R., Grant, J.A.,
         Guinness, E.A., Herkenhoff, K.E., Hurowitz, J.A., Johnson, J.R., Klingelhöfer, G., Lewis, K.W.,
         Li, R., McCoy, T.J., Moersch, J., McSween, H.Y., Murchie, S.L., Schmidt, M., Schröder, C.,
         Wang, A., Wiseman, S., Madsen, M.B., Goetz, W., McLennan, S.M., 2008. Spirit Mars Rover
         Mission to the Columbia Hills, Gusev Crater: Mission overview and selected results from the
         Cumberland Ridge to Home Plate. Journal of Geophysical Research 113.
         doi:10.1029/2008JE003183
Bibring, J.-P., 2006. Global Mineralogical and Aqueous Mars History Derived from OMEGA/Mars
         Express Data. Science 312, 400–404. doi:10.1126/science.1122659
Bibring, J.-P., Arvidson, R.E., Gendrin, A., Gondet, B., Langevin, Y., Le Mouelic, S., Mangold, N., Morris,
         R.V., Mustard, J.F., Poulet, F., Quantin, C., Sotin, C., 2007. Coupled Ferric Oxides and Sulfates
         on the Martian Surface. Science 317, 1206–1210. doi:10.1126/science.1144174
Bish, D.L., Howard, S.A., 1988. Quantitative phase analysis using the Rietveld method. Journal of Applied
         Crystallography 21, 86–91. doi:10.1107/S0021889887009415
Bishop, J.L., Loizeau, D., McKeown, N.K., Saper, L., Dyar, M.D., Des Marais, D.J., Parente, M., Murchie,
         S.L., 2013. What the ancient phyllosilicates at Mawrth Vallis can tell us about possible
         habitability on early Mars. Planetary and Space Science 86, 130–149.
         doi:10.1016/j.pss.2013.05.006
Bristow, T.F., Bish, D.L., Vaniman, D.T., Morris, R.V., Blake, D.F., Grotzinger, J.P., Rampe, E.B., Crisp,
         J.A., Achilles, C.N., Ming, D.W., Ehlmann, B.L., King, P.L., Bridges, J.C., Eigenbrode, J.L.,
         Sumner, D.Y., Chipera, S.J., Moorokian, J.M., Treiman, A.H., Morrison, S.M., Downs, R.T.,
         Farmer, J.D., Marais, D.D., Sarrazin, P., Floyd, M.M., Mischna, M.A., McAdam, A.C., 2015. The
         origin and implications of clay minerals from Yellowknife Bay, Gale crater, Mars. American
         Mineralogist 100, 824–836. doi:10.2138/am-2015-5077CCBYNCND
Burns, R.G., 1993. Rates and mechanisms of chemical weathering of ferromagnesian silicate minerals on
         Mars. Geochimica et Cosmochimica Acta 57, 4555–4574. doi:10.1016/0016-7037(93)90182-V

1177 Burns, R.G., 1987. Gossans on Mars. 18th Lunar and Planetary Science Conference 713–721.
1178 Carter, J., Poulet, F., Bibring, J.-P., Mangold, N., Murchie, S., 2013. Hydrous minerals on Mars as seen by
1179   the CRISM and OMEGA imaging spectrometers: Updated global view: HYDROUS MINERALS
1180   ON MARS: GLOBAL VIEW. Journal of Geophysical Research: Planets 118, 831–858.
1181   doi:10.1029/2012JE004145
1182 Cavanagh, P.D., Bish, D.L., Blake, D.F., Vaniman, D.T., Morris, R.V., Ming, D.W., Rampe, E.B., Achilles,
1183   C.N., Chipera, S.J., Treiman, A.H., Downs, R.T., Morrison, S.M., Fendrich, K.V., Yen, A.S.,
1184   Grotzinger, J., Crisp, J.A., Bristow, T.F., Sarrazin, P., Farmer, J.D., Des Marais, Stolper, E.,
1185   Morookian, J.M., Wilson, M.A., Spanovich, N., Anderson, R., 2015. Confidence Hills Mineralogy
1186   and CheMin Results from Base of Mt. Sharp, Pahrump Hills, Gale Crater, Mars. 46th Lunar and
1187   Planetary Science Conference Abstract #2735.
1188 Chemtob, S.M., Arvidson, R.E., FernáNdez-Remolar, D., Amils, R., 2006. Identification of Hydrated
1189   Sulfates Collected in the Northern Rio Tinto Valley by Reflectance and Raman Spectroscopy.
1190   Lunar and Planetary Science XXXVII Abstract 1941.
1191 Clark, R.N., Roush, T.L., 1984. Reflectance spectroscopy: Quantitative analysis techniques for remote
1192   sensing applications. Journal of Geophysical Research 89, 6329. doi:10.1029/JB089iB07p06329
1193 Dixon, E.M., Elwood Madden, A.S., Hausrath, E.M., Elwood Madden, M.E., 2015. Assessing
1194   hydrodynamic effects on jarosite dissolution rates, reaction products, and preservation on Mars:
1195   Hydrodynamics effects Mars Minerals. Journal of Geophysical Research: Planets 120, 625–642.
1196   doi:10.1002/2014JE004779
1197 Ehlmann, B.L., Mustard, J.F., Murchie, S.L., Bibring, J.-P., Meunier, A., Fraeman, A.A., Langevin, Y.,
1198   2011. Subsurface water and clay mineral formation during the early history of Mars. Nature 479,
1199   53–60. doi:10.1038/nature10582
1200 Ehlmann, B.L., Mustard, J.F., Swayze, G.A., Clark, R.N., Bishop, J.L., Poulet, F., Des Marais, D.J., Roach,
1201   L.H., Milliken, R.E., Wray, J.J., Barnouin-Jha, O., Murchie, S.L., 2009. Identification of hydrated
1202   silicate minerals on Mars using MRO-CRISM: Geologic context near Nili Fossae and implications
1203   for aqueous alteration. Journal of Geophysical Research 114. doi:10.1029/2009JE003339
1204 Elwood Madden, M.E., Bodnar, R.J., Rimstidt, J.D., 2004. Jarosite as an indicator of water-limited
1205   chemical weathering on Mars. Nature 431, 821–823. doi:10.1038/nature02971
1206 Farrand, W.H., Glotch, T.D., Rice, J.W., Hurowitz, J.A., Swayze, G.A., 2009. Discovery of jarosite within
1207   the Mawrth Vallis region of Mars: Implications for the geologic history of the region. Icarus 204,
1208   478–488. doi:10.1016/j.icarus.2009.07.014
1209 Fernández-Remolar, D.C., 2003. Geological record of an acidic environment driven by iron
1210   hydrochemistry: The Tinto River system. Journal of Geophysical Research 108.
1211   doi:10.1029/2002JE001918
1212 Fernández-Remolar, D.C., Knoll, A.H., 2008. Fossilization potential of iron-bearing minerals in acidic
1213   environments of Rio Tinto, Spain: Implications for Mars exploration. Icarus 194, 72–85.
1214   doi:10.1016/j.icarus.2007.10.009
1215 Fernández-Remolar, D.C., Morris, R.V., Gruener, J.E., Amils, R., Knoll, A.H., 2005. The Río Tinto Basin,
1216   Spain: Mineralogy, sedimentary geobiology, and implications for interpretation of outcrop rocks at
1217   Meridiani Planum, Mars. Earth and Planetary Science Letters 240, 149–167.
1218   doi:10.1016/j.epsl.2005.09.043
1219 Fernández-Remolar, D.C., Prieto-Ballesteros, O., Gómez-Ortíz, D., Fernández-Sampedro, M., Sarrazin, P.,
1220   Gailhanou, M., Amils, R., 2011. Río Tinto sedimentary mineral assemblages: A terrestrial
1221   perspective that suggests some formation pathways of phyllosilicates on Mars. Icarus 211, 114–
1222   138. doi:10.1016/j.icarus.2010.09.008
1223 Fialips, C.-I., Petit, S., Decarreau, A., Beaufort, D., 2000. Influence of synthesis pH on kaolinite
1224   "crystallinity" and surface properties. Clays and Clay Minerals 48, 173–184.
1225 Gendrin, A., 2005. Sulfates in Martian Layered Terrains: The OMEGA/Mars Express View. Science 307,
1226   1587–1591. doi:10.1126/science.1109087
1227 Golden, D.C., Ming, D.W., Morris, R.V., Mertzman, S.A., 2005. Laboratory-simulated acid-sulfate
1228   weathering of basaltic materials: Implications for formation of sulfates at Meridiani Planum and
1229   Gusev crater, Mars. Journal of Geophysical Research 110. doi:10.1029/2005JE002451
1230 Graff, T.G., Morris, R.V., Achilles, C.N., Agresti, A.G., Ming, D.W., Hamilton, J.C., Mertzman, S.A.,
1231   Smith, J., 2012. Chemical and Mineralogical Characterization of Acid-Sulfate Alteration of

1232   Basaltic Material on Mauna Kea Volcano, Hawaii: Jarosite and Hydrated Halloysite. Lunar and
1233   Planetary Science XLIII Abstract, 2639.
1234 Grotzinger, J.P., Arvidson, R.E., Bell, J.F., Calvin, W., Clark, B.C., Fike, D.A., Golombek, M., Greeley,
1235   R., Haldemann, A., Herkenhoff, K.E., Jolliff, B.L., Knoll, A.H., Malin, M., McLennan, S.M.,
1236   Parker, T., Soderblom, L., Sohl-Dickstein, J.N., Squyres, S.W., Tosca, N.J., Watters, W.A., 2005.
1237   Stratigraphy and sedimentology of a dry to wet eolian depositional system, Burns formation,
1238   Meridiani Planum, Mars. Earth and Planetary Science Letters 240, 11–72.
1239   doi:10.1016/j.epsl.2005.09.039
1240 Grotzinger, J.P., Gupta, S., Malin, M.C., Rubin, D.M., Schieber, J., Siebach, K., Sumner, D.Y., Stack,
1241   K.M., Vasavada, A.R., Arvidson, R.E., Calef, F., Edgar, L., Fischer, W.F., Grant, J.A., Griffes, J.,
1242   Kah, L.C., Lamb, M.P., Lewis, K.W., Mangold, N., Minitti, M.E., Palucis, M., Rice, M.,
1243   Williams, R.M.E., Yingst, R.A., Blake, D., Blaney, D., Conrad, P., Crisp, J., Dietrich, W.E.,
1244   Dromart, G., Edgett, K.S., Ewing, R.C., Gellert, R., Hurowitz, J.A., Kocurek, G., Mahaffy, P.,
1245   McBride, M.J., McLennan, S.M., Mischna, M., Ming, D., Milliken, R., Newsom, H., Oehler, D.,
1246   Parker, T.J., Vaniman, D., Wiens, R.C., Wilson, S.A., 2015. Deposition, exhumation, and
1247   paleoclimate of an ancient lake deposit, Gale crater, Mars. Science 350, aac7575–aac7575.
1248   doi:10.1126/science.aac7575
1249 Grotzinger, J.P. et al., 2014. A Habitable Fluvio-Lacustrine Environment at Yellowknife Bay, Gale Crater,
1250   Mars. Science 343, 1242777–1242777. doi:10.1126/science.1242777
1251 Hurowitz, J.A., Fischer, W.W., Tosca, N.J., Milliken, R.E., 2010. Origin of acidic surface waters and the
1252   evolution of atmospheric chemistry on early Mars. Nature Geoscience 3, 323–326.
1253   doi:10.1038/ngeo831
1254 Hurowitz, J.A., Tosca, N.J., Dyar, M.D., 2009. Acid production by FeSO4{middle dot}nH2O dissolution
1255   and implications for terrestrial and martian aquatic systems. American Mineralogist 94, 409–414.
1256   doi:10.2138/am.2009.3085
1257 Klingelhofer, G., 2004. Jarosite and Hematite at Meridiani Planum from Opportunity's Mossbauer
1258   Spectrometer. Science 306, 1740–1745. doi:10.1126/science.1104653
1259 Langevin, Y., 2005. Sulfates in the North Polar Region of Mars Detected by OMEGA/Mars Express.
1260   Science 307, 1584–1586. doi:10.1126/science.1109091
1261 Lichtenberg, K.A., Arvidson, R.E., Morris, R.V., Murchie, S.L., Bishop, J.L., Fernandez Remolar, D.,
1262   Glotch, T.D., Noe Dobrea, E., Mustard, J.F., Andrews-Hanna, J., Roach, L.H., 2010. Stratigraphy
1263   of hydrated sulfates in the sedimentary deposits of Aram Chaos, Mars. Journal of Geophysical
1264   Research 115. doi:10.1029/2009JE003353
1265 Madejová, J., Pentrák, M., Pálková, H., Komadel, P., 2009. Near-infrared spectroscopy: A powerful tool in
1266   studies of acid-treated clay minerals. Vibrational Spectroscopy 49, 211–218.
1267   doi:10.1016/j.vibspec.2008.08.001
1268 Metz, J., Grotzinger, J., Okubo, C., Milliken, R., 2010. Thin-skinned deformation of sedimentary rocks in
1269   Valles Marineris, Mars. Journal of Geophysical Research 115. doi:10.1029/2010JE003593
1270 Metz, J.M., Grotzinger, J.P., Mohrig, D., Milliken, R., Prather, B., Pirmez, C., McEwen, A.S., Weitz, C.M.,
1271   2009. Sublacustrine depositional fans in southwest Melas Chasma. Journal of Geophysical
1272   Research 114. doi:10.1029/2009JE003365
1273 Michalski, J.R., Niles, P.B., Cuadros, J., Baldridge, A.M., 2013. Multiple working hypotheses for the
1274   formation of compositional stratigraphy on Mars: Insights from the Mawrth Vallis region. Icarus 226,
1275   816–840. doi:10.1016/j.icarus.2013.05.024
1276 Milliken, R.E., Swayze, G.A., Arvidson, R.E., Bishop, J.L., Clark, R.N., Ehlmann, B.L., Green, R.O.,
1277   Grotzinger, J.P., Morris, R.V., Murchie, S.L., Mustard, J.F., Weitz, C., 2008. Opaline silica in
1278   young deposits on Mars. Geology 36, 847. doi:10.1130/G24967A.1
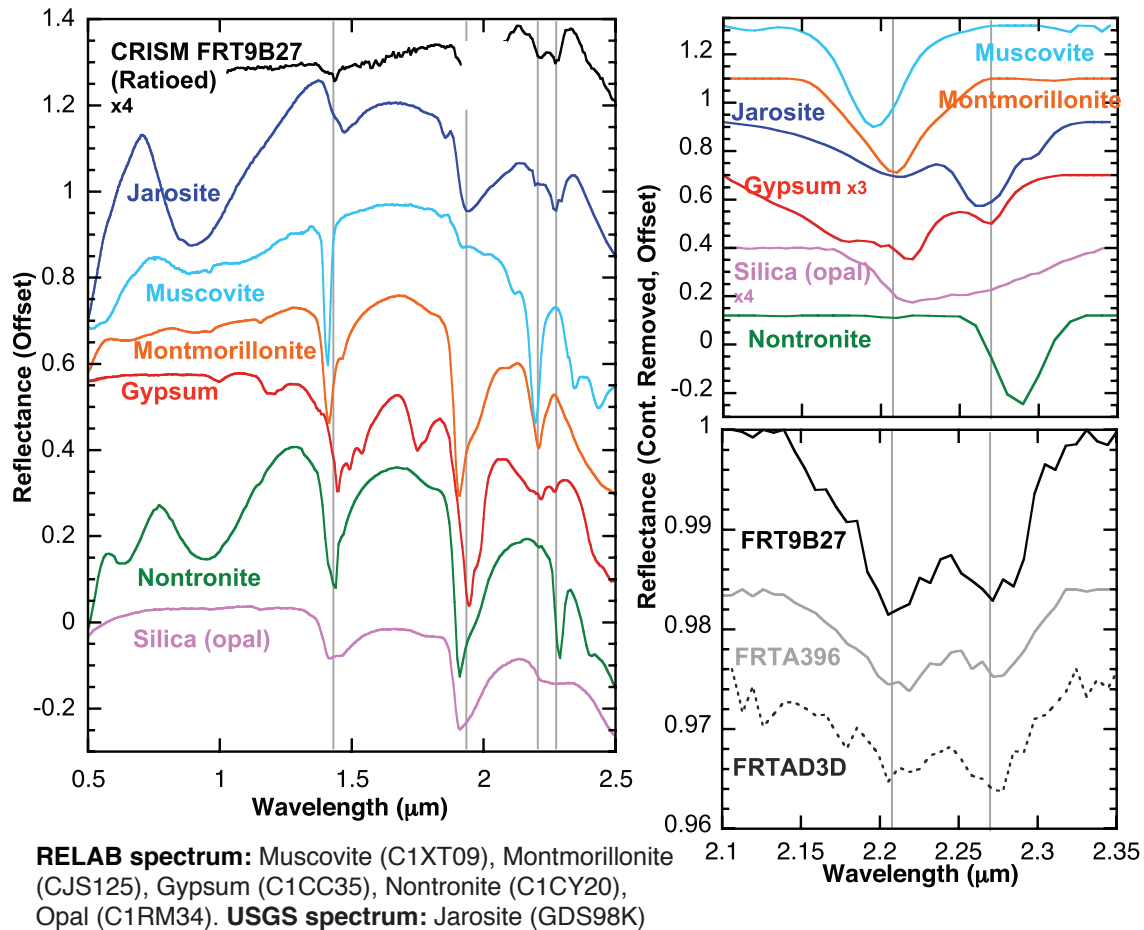1279 Murchie, S., Arvidson, R., Bedini, P., Beisser, K., Bibring, J.-P., Bishop, J., Boldt, J., Cavender, P., Choo,
1280   T., Clancy, R.T., Darlington, E.H., Des Marais, D., Espiritu, R., Fort, D., Green, R., Guinness, E.,
1281   Hayes, J., Hash, C., Heffernan, K., Hemmler, J., Heyler, G., Humm, D., Hutcheson, J., Izenberg,
1282   N., Lee, R., Lees, J., Lohr, D., Malaret, E., Martin, T., McGovern, J.A., McGuire, P., Morris, R.,
1283   Mustard, J., Pelkey, S., Rhodes, E., Robinson, M., Roush, T., Schaefer, E., Seagrave, G., Seelos,
1284   F., Silverglate, P., Slavney, S., Smith, M., Shyong, W.-J., Strohbehn, K., Taylor, H., Thompson,
1285   P., Tossman, B., Wirzburger, M., Wolff, M., 2007. Compact Reconnaissance Imaging
1286   Spectrometer for Mars (CRISM) on Mars Reconnaissance Orbiter (MRO). Journal of Geophysical
1287   Research 112. doi:10.1029/2006JE002682

Mustard, J.F., Murchie, S.L., Pelkey, S.M., Ehlmann, B.L., Milliken, R.E., Grant, J.A., Bibring, J.-P., Poulet, F., Bishop, J., Dobrea, E.N., Roach, L., Seelos, F., Arvidson, R.E., Wiseman, S., Green, R., Hash, C., Humm, D., Malaret, E., McGovern, J.A., Seelos, K., Clancy, T., Clark, R., Marais, D.D., Izenberg, N., Knudson, A., Langevin, Y., Martin, T., McGuire, P., Morris, R., Robinson, M., Roush, T., Smith, M., Swayze, G., Taylor, H., Titus, T., Wolff, M., 2008. Hydrated silicate minerals on Mars observed by the Mars Reconnaissance Orbiter CRISM instrument. Nature 454, 305–309. doi:10.1038/nature07097

Noe Dobrea, E., Michalski, J.R., Swayze, G.A., 2011. Aqueous Mineralogy and Stratigraphy at and Around the Proposed Mawrth Vallis MSL Landing Site: New Insights into the Aqueous History of the Region. The International Journal of Mars Science and Exploration 6, 32–46.

Pelkey, S.M., Mustard, J.F., Murchie, S., Clancy, R.T., Wolff, M., Smith, M., Milliken, R., Bibring, J.-P., Gendrin, A., Poulet, F., Langevin, Y., Gondet, B., 2007. CRISM multispectral summary products: Parameterizing mineral diversity on Mars from reflectance. Journal of Geophysical Research 112. doi:10.1029/2006JE002831

Poulet, F., Bibring, J.-P., Mustard, J.F., Gendrin, A., Mangold, N., Langevin, Y., Arvidson, R.E., Gondet, B., Gomez, C., Berthé, M., Bibring, J.-P., Langevin, Y., Erard, S., Forni, O., Gendrin, A., Gondet, B., Manaud, N., Poulet, F., Poulleau, G., Soufflot, A., Combes, M., Drossart, P., Encrenaz, T., Fouchet, T., Melchiorri, R., Bellucci, G., Altieri, F., Formisano, V., Fonti, S., Capaccioni, F., Cerroni, P., Coradini, A., Korablev, O., Kottsov, V., Ignatiev, N., Titov, D., Zasova, L., Mangold, N., Pinet, P., Schmitt, B., Sotin, C., Hauber, E., Hoffmann, H., Jaumann, R., Keller, U., Arvidson, R., Mustard, J., Forget, F., 2005. Phyllosilicates on Mars and implications for early martian climate. Nature 438, 623–627. doi:10.1038/nature04274

Roach, L.H., Mustard, J., Gendrin, A., Fernández-Remolar, D., Amils, R., Amaral-Zettler, L., 2006. Finding mineralogically interesting targets for exploration from spatially coarse visible and near IR spectra. Earth and Planetary Science Letters 252, 201–214. doi:10.1016/j.epsl.2006.09.044

Roach, L.H., Mustard, J.F., Swayze, G., Milliken, R.E., Bishop, J.L., Murchie, S.L., Lichtenberg, K., 2010. Hydrated mineral stratigraphy of Ius Chasma, Valles Marineris. Icarus 206, 253–268. doi:10.1016/j.icarus.2009.09.003

Sobron, P., Bishop, J.L., Blake, D.F., Chen, B., Rull, F., 2014. Natural Fe-bearing oxides and sulfates from the Rio Tinto Mars analog site: Critical assessment of VNIR reflectance spectroscopy, laser Raman spectroscopy, and XRD as mineral identification tools. American Mineralogist 99, 1199–1205. doi:10.2138/am.2014.4595

Sobron, P., Sanz, A., Acosta, T., Rull, F., 2009. A Raman spectral study of stream waters and efflorescent salts in Rio Tinto, Spain. Spectrochimica Acta Part A: Molecular and Biomolecular Spectroscopy 71, 1678–1682. doi:10.1016/j.saa.2008.06.035

Squyres, S.W., 2004. In Situ Evidence for an Ancient Aqueous Environment at Meridiani Planum, Mars. Science 306, 1709–1714. doi:10.1126/science.1104559

Sunshine, J.M., Pieters, C.M., 1993. Estimating Modal Abundances From the Spectra of Natural and Laboratory Pyroxene Mixtures Using the Modified Gaussian Model. Journal of Geophysical Research 98, 9075–9087.

Thollot, P., Mangold, N., Ansan, V., Le Mouélic, S., Milliken, R.E., Bishop, J.L., Weitz, C.M., Roach, L.H., Mustard, J.F., Murchie, S.L., 2012. Most Mars minerals in a nutshell: Various alteration phases formed in a single environment in Noctis Labyrinthus: ALTERATION PHASES IN NOCTIS LABYRINTHUS. Journal of Geophysical Research: Planets 117, n/a–n/a. doi:10.1029/2011JE004028

Tosca, N.J., 2004. Acid-sulfate weathering of synthetic Martian basalt: The acid fog model revisited. Journal of Geophysical Research 109. doi:10.1029/2003JE002218

Tosca, N.J., Knoll, A.H., McLennan, S.M., 2008a. Water Activity and the Challenge for Life on Early Mars. Science 320, 1204–1207. doi:10.1126/science.1155432

Tosca, N.J., McLennan, S.M., 2006. Chemical divides and evaporite assemblages on Mars. Earth and Planetary Science Letters 241, 21–31. doi:10.1016/j.epsl.2005.10.021

Tosca, N.J., Milliken, R.E., Michel, F.M., 2008b. Smectite Formation on Early Mars: Experimental Constraints. Martian Phyllosilicates: Recorders of Aqueous Processes Abstract, 7030.

Vaniman, D.T. et al., 2014. Mineralogy of a Mudstone at Yellowknife Bay, Gale Crater, Mars. Science 343, 1243480–1243480. doi:10.1126/science.1243480

1343 Wang, A., Korotev, R.L., Jolliff, B.L., Haskin, L.A., Crumpler, L., Farrand, W.H., Herkenhoff, K.E., de
1344   Souza, P., Kusack, A.G., Hurowitz, J.A., Tosca, N.J., 2006. Evidence of phyllosilicates in Wooly
1345   Patch, an altered rock encountered at West Spur, Columbia Hills, by the Spirit rover in Gusev
1346   crater, Mars. Journal of Geophysical Research 111. doi:10.1029/2005JE002516
1347 Weitz, C.M., Bishop, J.L., Thollot, P., Mangold, N., Roach, L.H., 2011. Diverse mineralogies in two
1348   troughs of Noctis Labyrinthus, Mars. Geology 39, 899–902. doi:10.1130/G32045.1
1349 Weitz, C.M., Noe Dobrea, E., Wray, J.J., 2014. Mixtures of clays and sulfates within deposits in western
1350   Melas Chasma, Mars. Icarus. doi:10.1016/j.icarus.2014.04.009
1351
1352
1353 **Figures**

RELAB spectrum: Muscovite (C1XT09), Montmorillonite (CJS125), Gypsum (C1CC35), Nontronite (C1CY20), Opal (C1RM34). **USGS spectrum:** Jarosite (GDS98K)

1354
1355 **Figure 1:** Reflectance spectra of minerals with absorptions between 2.2 and 2.3 μm
1356 (source: RELAB database) are compared to CRISM spectra showing the 'doublet'
1357 absorption. Continuum-removed spectra from 2.1 to 2.35 μm (right) are shown to
1358 highlight absorption features in the wavelength region where the doublet occurs.
1359 None of the pure mineral spectra have absorption positions and depths that are a
1360 direct match to the doublet absorptions, thus a mineral mixture is implied.
1361

Sample ID	Location	Terrace	Spectral Doublet	Reitveld Refinement
RT1	Berrocal	Modern		
RT2	Berrocal	Modern		
RT3	Berrocal	Modern		
RT4 (mud, loose)	Berrocal	Modern		
RT5	Anabel's Garden, Upper Road	N/A		
RT6	Anabel's Garden, Upper Road	N/A		
RT7	Anabel's Garden, Upper Road	N/A		Yes
RT8	Anabel's Garden, Upper Road	N/A		
RT9	Anabel's Garden, Upper Road	N/A	Yes	Yes
RT10	Anabel's Garden, Upper Road	N/A	Yes	Yes
RT11	Anabel's Garden, Upper Road	N/A	Yes	Yes
RT12	Barranco de los Locos	Lower Terrace	Yes	Yes
RT13	Barranco de los Locos	Lower Terrace		
RT14	Barranco de los Locos	Lower Terrace		
RT15	Barranco de los Locos	Lower Terrace	Yes	Yes
RT16	Anabel's Garden, Stream 1	Modern	Yes	Yes
RT17 (precipitate)	Anabel's Garden, Stream 2	Modern		
RT18 (precipitate)	Anabel's Garden, Stream 2	Modern		
RT19	Anabel's Garden, Stream 2	Modern	Yes	Yes
RT20 (precipitate)	Anabel's Garden, Stream 2	Modern		
RT21	Anabel's Garden, Stream 2	Modern		
RT22	Anabel's Garden, Stream 2	Modern		
RT23	Anabel's Garden, Stream 2	Modern		Yes
RT24	Source Spring	Modern		
RT25	Source Spring	Modern		
RT26	Source Spring	Modern	Yes	Yes
RT27 (precipitate)	Source Spring	Modern		
RT28	Alta de la Mesa	Upper Terrace		
RT29	Alta de la Mesa	Upper Terrace		
RT30	Alta de la Mesa	Upper Terrace		Yes
RT31	Alta de la Mesa	Upper Terrace		
RT32	Gossan outcrop	N/A		
RT33	Gossan outcrop	N/A		
RT34	Gossan outcrop	N/A		

1362
1363
1364 **Table 1:** A full list of samples collected at the modern streambed, lower and upper
1365 terraces at Rio Tinto. All samples are rocks unless otherwise noted. Each sample is
1366 measured with the ASD, FTIR, and XRD in the laboratory. Samples with a spectral
1367 doublet and those that have been analyzed with a Rietveld refinement are noted.
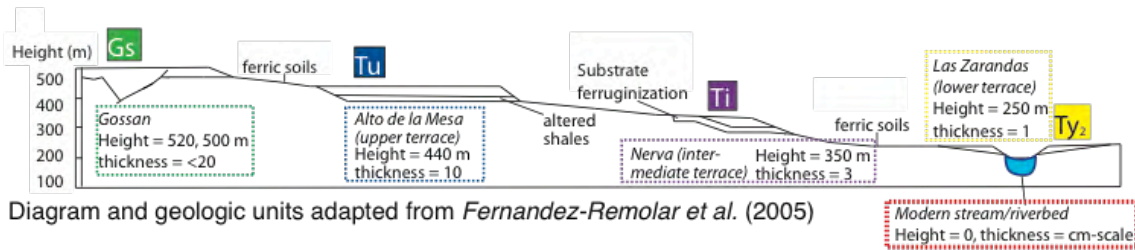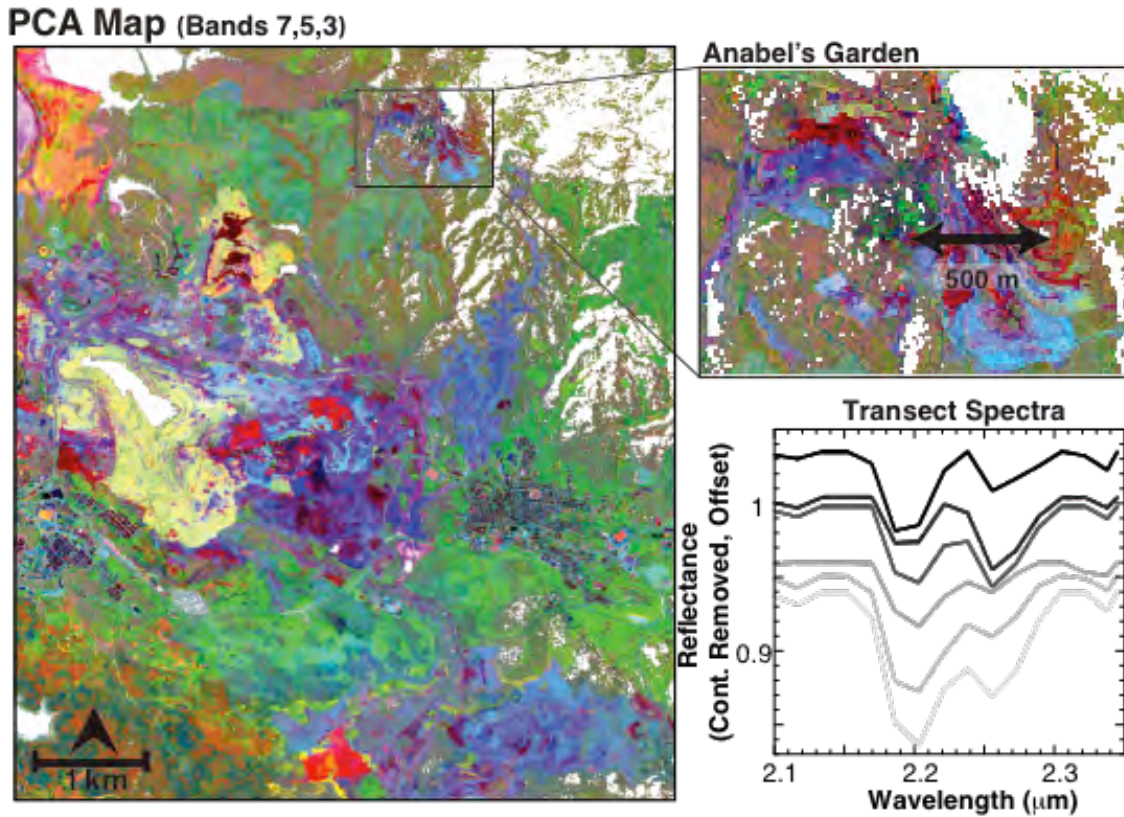1368

Figure 2: Terraces of the Rio Tinto in the schematic diagram from Fernandez-Remolar et al. (2005) are matched with locations in the HyMap aerial hyperspectral image of the region that were sampled in this study.

1374

1375
Figure 3: A principal components analysis has been carried out on the same HyMap
image as seen in Figure 2, and like colors in the image correspond to regions of
spectral similarity (R = PCA band 7, G = band 3, B = band 5). The spectral doublet is
associated with units that appear in a dark red color in this false-color image, which
is particularly evident at Anabel's Garden (inset) where a number of the doublet-
bearing samples were collected. Variation in the spectral doublet from 2.2 – 2.3 μm
is highlighted with spectra collected from a 500 m HyMap transect (black arrow).

| Sample			Rietveld Results				XRD Peak Areas	
Sample	Location	Doublet?	Jarosite (wt%)	Muscovite (wt%)	Illite (wt%)	R_{wp}	Peak area: Musc/Ill	Peak area: Jarosite
RT9	AG Mining Terrace	Yes	3	16	14	5.61	1717.8	639
RT10	AG Mining Terrace	Yes	7	46	0	5.01	2438.3	673.4
RT11	AG Mining Terrace	Yes	4	24	0	5.52	1239.4	573.1
RT12	Barranco de los Locos	Yes	11	13	0	1.12	2115.3	1956.1
RT15	Barranco de los Locos	Yes	37	12	0	1.21	2089.9	2050.9
RT16	Anabel's Garden (Stream)	Yes	3	5	0	10.08	555.4	353.4
RT19	Anabel's Garden (stream)	Yes	3	0	19	3.16	536.3	464.9
RT26	Source Spring	Yes	8	50	0	2.52	4655.9	2959.1
RT30	Alta de la Mesa	No	0	0	0	3.67	0	0
RT23	Anabel's Garden (Stream)	No	32	0	0	1.66	0	1003.8
RT7	Anabel's Garden	No	0	0	4	1.03	432.1	0

1385

1386 **Table 2:** Sample IDs and origin of samples that were analyzed using XRD and
1387 reflectance spectroscopy. The jarosite and Al-clay (muscovite/illite) content of each
1388 sample was estimated using Rietveld refinement on the XRD patterns.
1389
1390
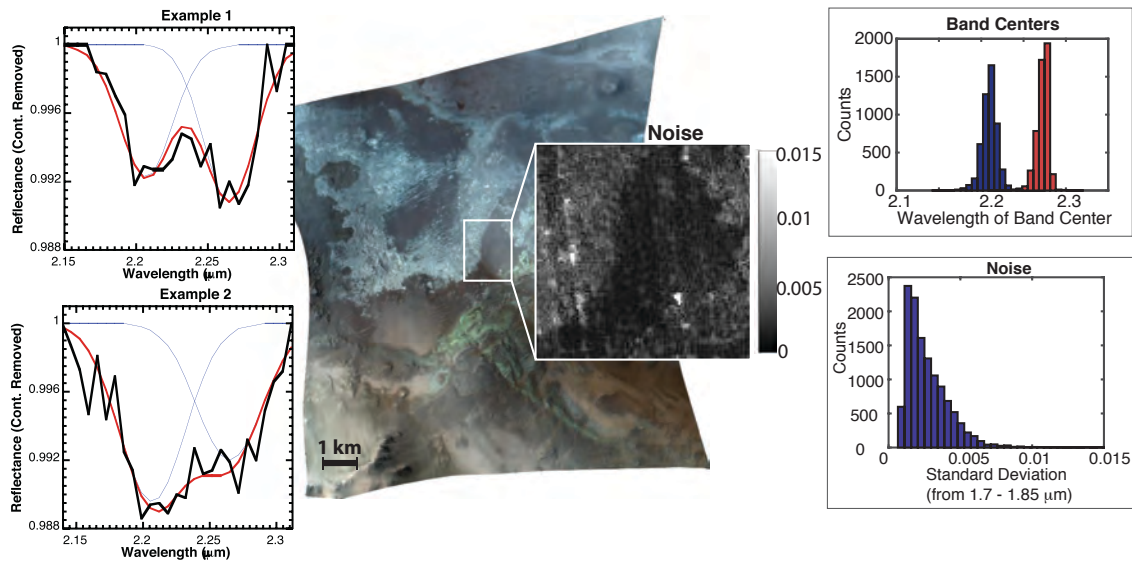
1391
1392 **Figure 4:** Two Gaussian fit examples are shown for FRT00009B27 from Ius Chasma,
1393 Mars. Due to noise in the spectrum, the Gaussian mean may be a better
1394 representative of band depth minimum than the true reflectance value. Noise and
1395 spectral smile are further analyzed for a central subset of the image. Noise is
1396 calculated as the standard deviation of a flat, absorption free portion of the
1397 spectrum from 1.7 – 1.85 μm. An image and histogram of this standard deviation
1398 show that noise is typically < 0.005 in reflectance. Band center histograms are also
1399 shown for the central image subset, and the reduced spread in band centers
1400 compared to the full image suggests spectral smile plays a role in the band center
1401 position.
1402

1403
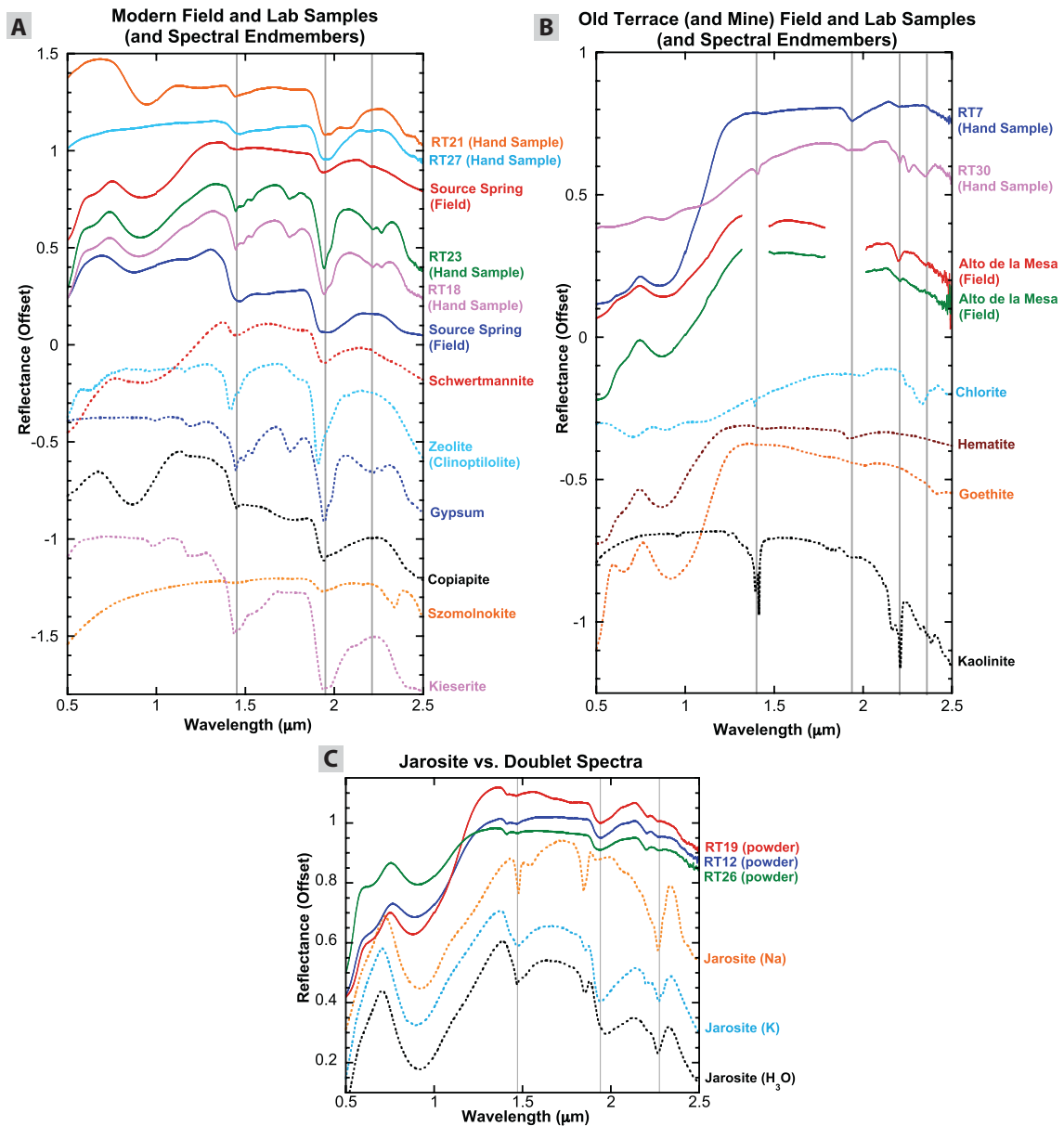
Figure 5: Example spectra from the field and laboratory for the A) modernly precipitating streambed at Rio Tinto (source region, which includes Source Spring, Richi Spring, and Anabel's Garden) and B) the ~2myr old terrace at Alto de la Mesa. These spectra show the transition from very hydrated, sulfate minerals to ferric oxides through time (with some clays possibly associated with mining activity). All of the mineralogies identified in hand samples are also found in the field spectra, but only a limited number of each is shown for the sake of clarity. In C), absorptions in powdered samples that show a doublet are specifically compared to jarosite spectral endmembers. Again, a very similar doublet signature is seen in both field and hand samples, but is not shown for clarity. Endmember mineral spectra from RELAB and USGS are shown for reference (RELAB: RM-JFM-036, RM-JFM-035, CC-JFM-013A, JB-JLB-752, JB-JLB-753, JB-JLB-757, JB-CMP-047, JB-CMP-054, CC-JFM-

1417   017-B, JB-JLB_256, CC-JFM-035, CL-TXH-014, JB-CMP-25-B; USGS: BZ93-1, GDS2

1418   Zeolite W1R1Bb)

1419
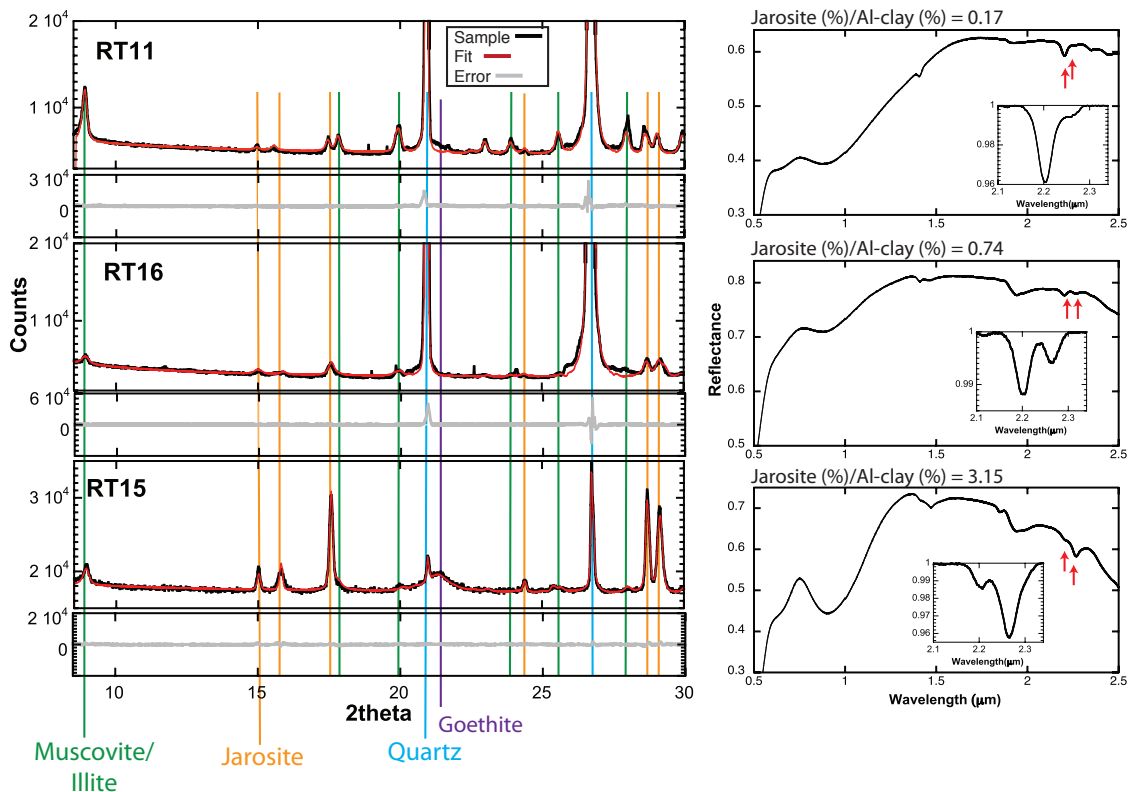
1420

1421   **Figure 6:** XRD patterns with corresponding reflectance spectra from three

1422   powdered samples with different proportions of jarosite and Al-clay (RT 11, RT15,

1423   RT16). Major phases are labeled for the XRD patterns and absorptions

1424   corresponding to the doublet feature are marked by red arrows in the reflectance

1425   spectra plots.

1426
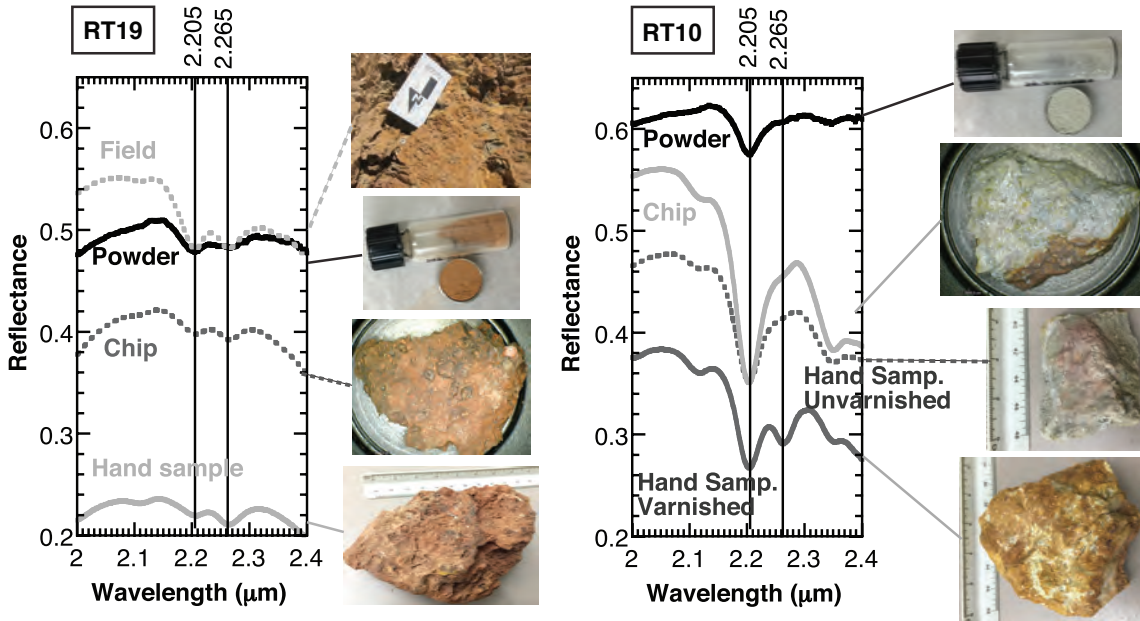
1427
1428 **Figure 7:** Example reflectance spectra acquired in the field and for hand sample,
1429 chip, and powder versions of two samples from different locations within the study
1430 region. Chips are <9 mm in diameter and powders were sieved to <45 μm. Spectra of
1431 these samples highlight the variation in absolute reflectance and band depth of the
1432 two absorptions in the doublet feature when measured at different spatial scales.
1433 Hand sample RT10 has a varnished surface for which the reflectance spectra exhibit
1434 a clear doublet feature, whereas spectra from the interior portions exhibit a much
1435 weaker long-wavelength (jarosite) absorption.
1436
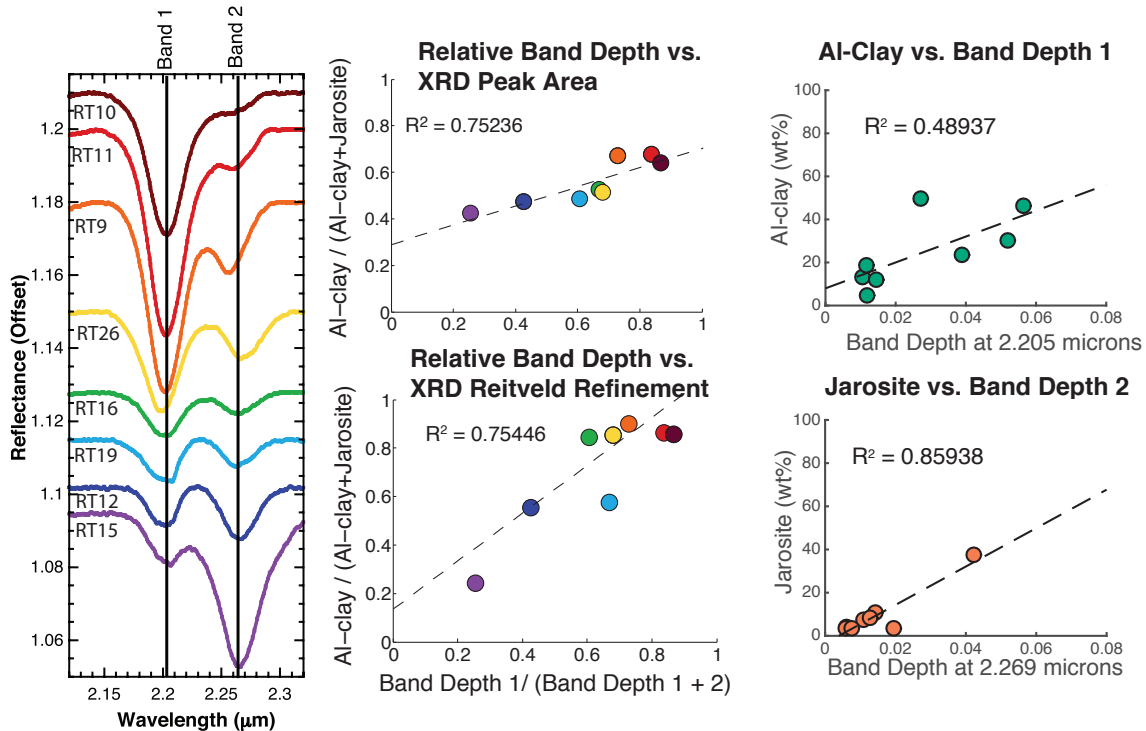
1437

1438 **Figure 8:** Comparison of XRD results with reflectance spectra (band depths) to
1439 show relationship between mineral abundances and the absorption feature
1440 strength. A direct relationship between relative amounts of jarosite and Al-clay and
1441 the strengths of the absorption features indicates the shorter wavelength
1442 absorption (band 1; ~2.21 μm) arises from Al-clay and the longer wavelength
1443 absorption (band 2; ~2.265) arises from the presence of jarosite. This suggests that
1444 relative band strengths are directly related to the relative proportions of the
1445 phyllosilicate and sulfate components.
1446

Image	Band 1 (μm)	2σ (μm)	Band 2 (μm)	2σ (μm)
Mars				
FRT00009B27 full image	2.2109	0.0264	2.2709	0.019
FRT00009B27 center	2.2006	0.0134	2.265	0.0112
FRT0000A396 full image	2.2048	0.0154	2.2696	0.0132
FRT0000A396 center	2.2055	0.0134	2.2705	0.0136
FRT0000AD3D full image	2.2055	0.0188	2.2662	0.0156
FRT0000AD3D center	2.2085	0.0142	2.2671	0.0108
Rio Tinto				
HyMap	2.2025	0.013	2.2602	0.011

1447
1448 **Table 3**: The results of Gaussian fits for every pixel in three CRISM images (Mars)
1449 and the HyMap image (Rio Tinto) that includes the mean band centers and the 2σ
1450 deviations on these band centers. A central subset of the CRISM images is also
1451 analyzed and reported results show a shift in band centers and a decrease in
1452 standard deviation.

1453

A

FRT00009B27   FRT0000A396   FRT0000AD3D

5 km   5 km   5 km

B

C

D
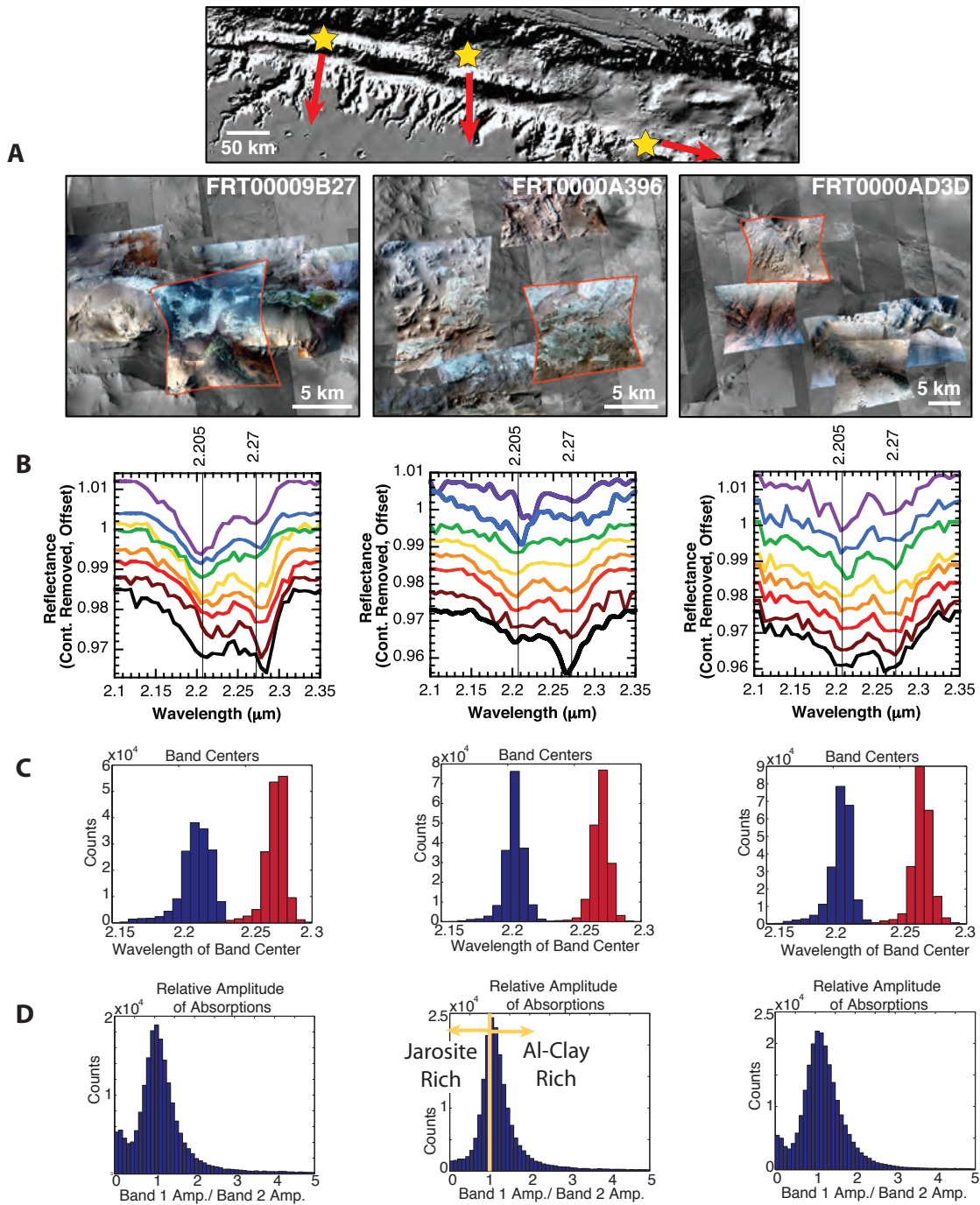
1454
Figure 9: Examples of doublet-bearing materials on Mars as observed in MRO
CRISM images. (A) MOLA hillshade image showing the location of three study
regions in Ius and Melas Chasma within the Valles Marineris. Zoom-in regions below
show locations of CRISM images FRT00009B27, FRT0000A396, and FRT0000AD3D
in context with nearby CRISM images (overlain on HiRISE and CTX images).
Doublet-bearing units in CRISM images 9B27 and AD3D are light toned and tend to
drape pre-existing topography; CRISM image A396 shows that the doublet-bearing

1462   material corresponds to a blocky, brecciated unit. (B) Examples of spectral variation
1463   within the doublet-bearing units, ranging from a stronger 2.205 μm absorption to a
1464   stronger 2.269 μm absorption. (C) Histograms showing positions of the 2.205 μm
1465   (blue) and 2.269 μm (red) band positions for every doublet-bearing pixel in each of
1466   the three images and (D) histograms showing the relative strength of the two
1467   absorption features (Band 1 = ~2.205 μm; Band 2 = ~2.269 μm). Values in (C) and
1468   (D) are based on Gaussian fits as described in the text. Data for each column in (B),
1469   (C), and (D) correspond to the CRISM FRT images labeled and highlighted in red in
1470   (A).
1471
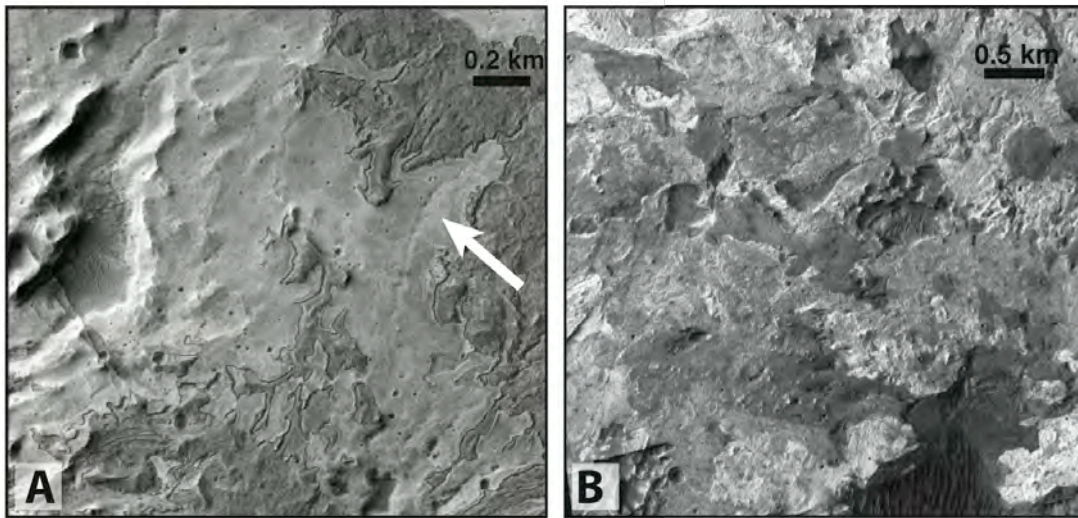
1472
1473   **Figure 10:** Examples of doublet-bearing units as observed in MRO HiRISE images.
1474   These units are typically light-toned, contorted and/or blocky in nature. (A)
1475   Example of a doublet-bearing unit in Melas Chasma that drapes pre-existing
1476   topography and spans a wide range in elevation. (B) An example of doublet-bearing,
1477   light-toned units that may have slumped off the canyon walls and are now part of a
1478   brecciated unit on the floor. The morphology and spectral characteristics of these
1479   and similar deposits are described in detail in Roach et al. (2010), Metz et al. (2010),
1480   and Weitz et al. (2014). (HiRISE images: (A) PSP_007074_1725, (B)
1481   PSP_007509_1720).

1482
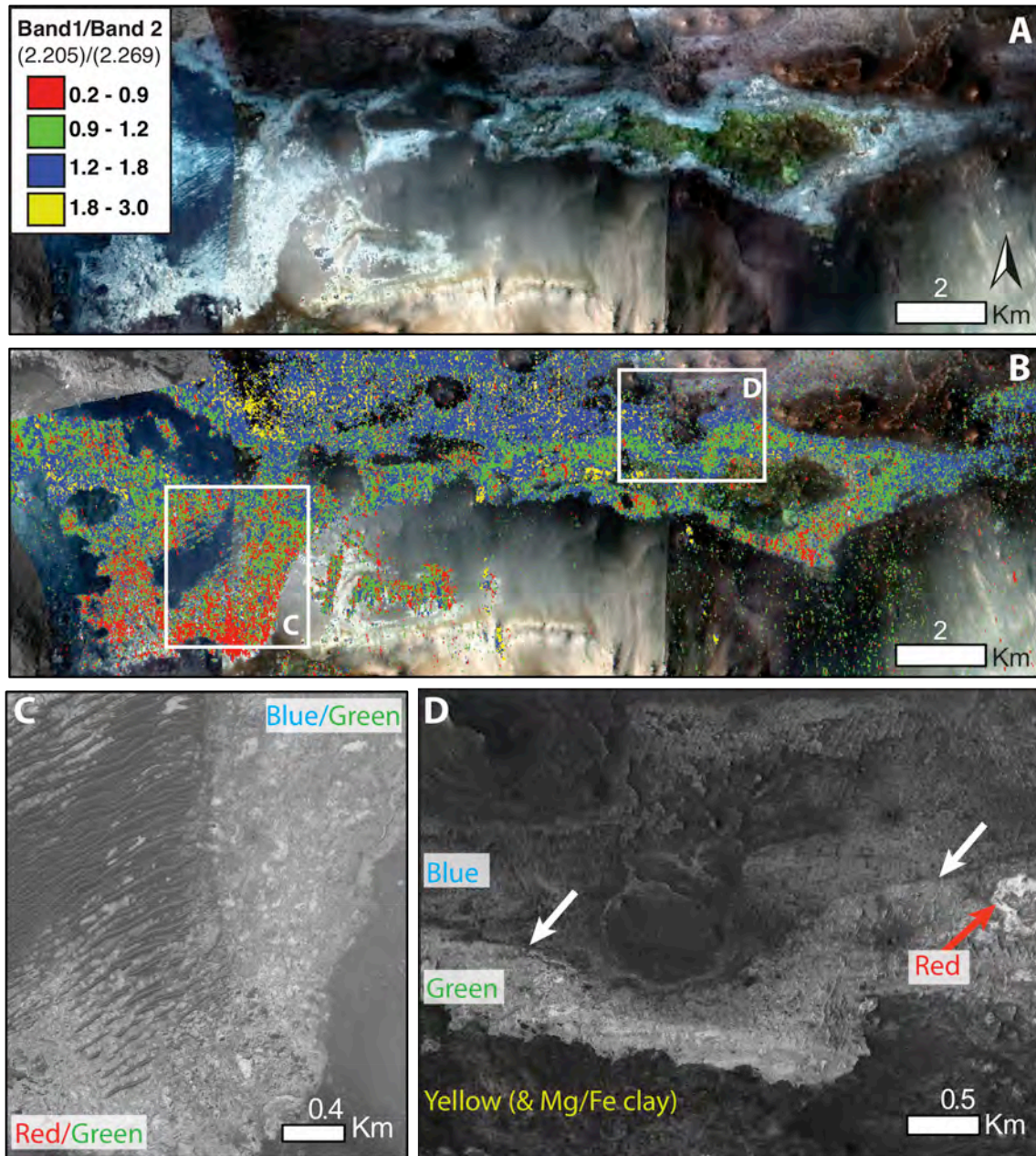
1483
1484 **Figure 11:** Relative amplitude of absorptions (band depth at 2.207/ band depth at
1485 2.269) in Ius Chasma and associated morphology. (A) False-color CRISM images (R –
1486 band 253, B – band 53, G = band 17, top) overlain on a CTX mosaic. Fe/Mg-clay
1487 bearing regions appear greenish in color and the doublet-bearing regions appear
1488 light-toned or white. (B) CRISM pixels with the doublet feature are highlighted by
1489 different colors that map the relative band strength of the two absorptions, with a
1490 gradient from more jarosite rich (red), to roughly equal jarosite/Al-phyllosilicate
1491 strength, to slightly more Al-phyllosilicate rich (blue), to very Al-phyllosilicate rich
1492 (yellow). (C) Close-up view of HiRISE image ESP_041121_1725 showing that there is
1493 no clear stratigraphic boundary associated with the transition from a more jarosite-

1494   rich "red" region to a more Al-phyllosilicate rich "blue" area in this location. (D)
1495   Close-up of HiRISE image PSP_007074_1725 showing an example where
1496   morphologically and stratigraphically distinct units correspond to the different
1497   relative band strengths. Here, white arrows indicate a clear stratigraphic boundary
1498   that also corresponds to a clear boundary between green and blue pixels seen in (B)
1499   (HiRISE images: ESP_041121_1725, PSP_007074_1725, CRISM images listed above).
1500
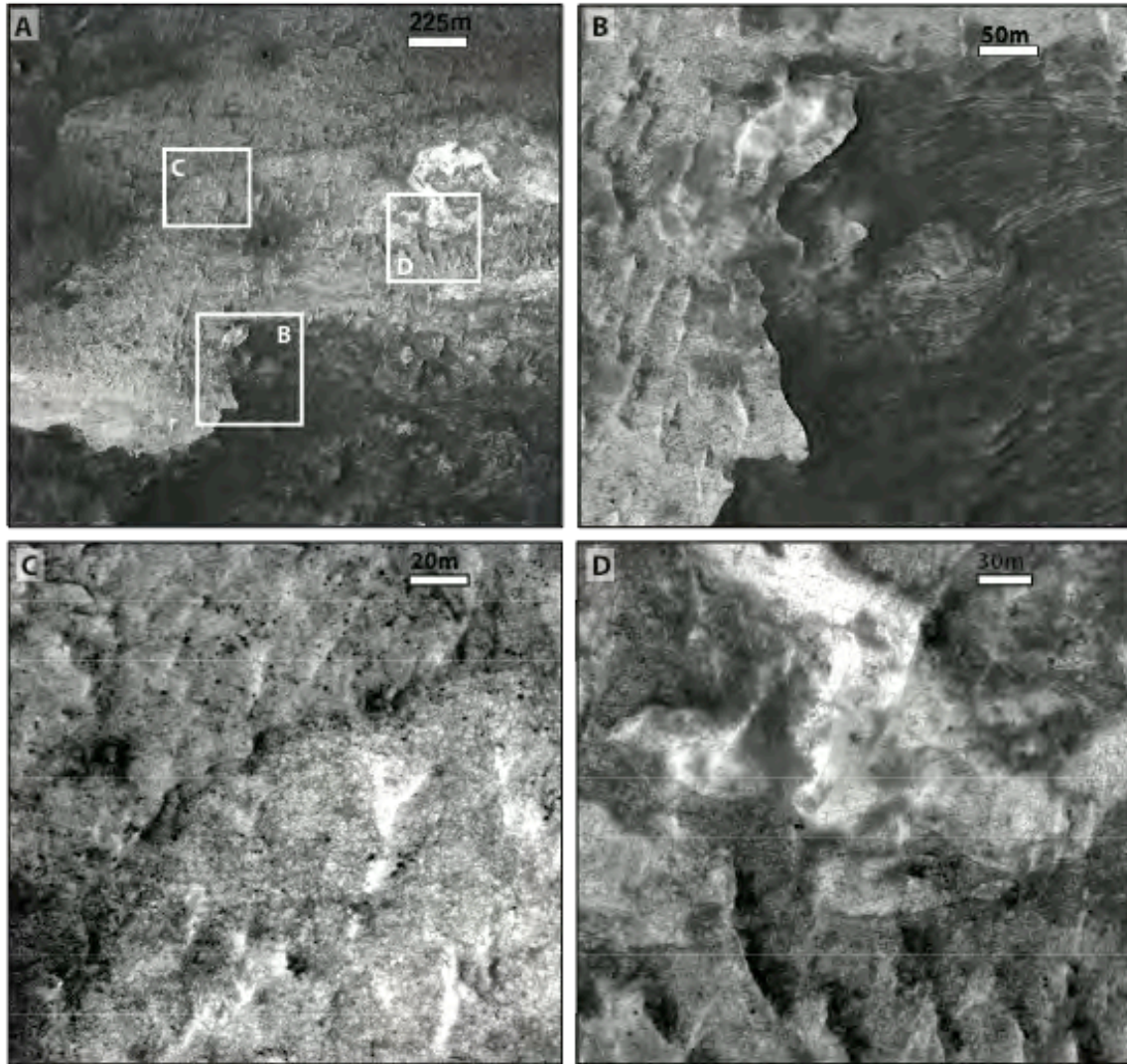
1501
1502 **Figure 12:** Evidence of the stratigraphic contacts between different doublet-bearing
1503   units that are identified as more jarosite- or Al-phyllosilicate-rich in the color map in
1504   Figure 11. (A) Context map from HiRISE image ESP_041121_1725 showing locations
1505   where three contacts are visible. (B) Shows the clay bearing unit (dark-toned,
1506   stratified with tilted bedding) unconformably overlain by the light-toned doublet
1507   unit, which has relative band strengths between 0.9 and 1.2 (i.e. the strength of the
1508   two absorptions in the doublet are similar). Next, in (C) there is a contact between
1509   this same light-toned unit and a slightly darker, more Al-phyllosilicate-rich unit,
1510   which appears to lie stratigraphically above it. Finally, (D) shows the contact
1511   between the brightest unit, which outcrops in smaller areas throughout Ius, and the

1512 light-toned doublet-bearing unit shown in (B) and (C). This bright unit is mapped as
1513 being more jarosite rich in Figure 8 and appears to be stratigraphically lower than
1514 the light-toned unit. It is not possible to determine the exact relationship between
1515 this bright material and the dark, stratified clay deposit in this location, but in other
1516 regions it appears as if the brightest (jarosite-rich) material is stratigraphically
1517 above the clay-bearing strata. Therefore, the increasing stratigraphic order appears
1518 to be: dark (clay-bearing) strata > brightest unit > light-toned unit > moderate-
1519 toned unit. The corresponding mineralogy is consistent with: clay-rich > more
1520 jarosite-rich > equal Al-phyllosilicate and jarosite > more Al-phyllosilicate rich (that
1521 is, within the doublet-bearing units the proportion of jarosite *decreases* upsection).
1522
1523
1524
1525
1526
1527
1528
1529
1530
1531
1532
1533
1534 **<u>Supplementary Material</u>**
1535
1536
1537
1538 **1. Methods**
1539
1540 Additional information from the methods section can be found here.
1541
1542
1543 *1.1. CRISM image processing and Gaussian fitting*
1544
1545   CRISM image cubes were corrected for atmospheric gases using the 'volcano

1546 scan' method described by Langevin et al. [2005] and Mustard et al. [2008]. All

1547 CRISM processing steps, including map-projection, were carried out with the freely

1548 available IDL CRISM Analysis Tools (CAT) [Pelkey et al., 2007] and the commercially

1549 available ENVI software package.

1550   CRISM spectra in regions of interest (ROIs) spanning ~100 to 1000 pixels

1551 were averaged to understand large-scale regional mineral assemblages. A spectrally

1552   bland or neutral ROI was chosen to represent background martian surface

1553   reflectance properties (e.g. martian dust), and every pixel within an image was

1554   divided by the spectrum corresponding to the neutral ROI within that same image.

1555   This method produces spectral ratios that highlight and accentuate reflectance

1556   properties of ROIs relative to those associated with typical martian dust and/or soil.

1557   Starting with the continuum-removed CRISM images, pixels whose spectra

1558   exceeded a user-defined (and image-dependent) band depth threshold at ~2.205

1559   μm were selected for Gaussian fitting. The threshold used here is band depth

1560   ≥0.005. Though it is not suggested that the same value can be used for every CRISM

1561   image due to differences in noise, for the images used in this study this value is

1562   larger than the background 'noise' in the ratio spectra. This was determined by

1563   calculating the mean and standard deviation over the 1.70-1.85 μm wavelength

1564   range (24 channels) for each ratio spectrum (pixel) in each CRISM image. This

1565   wavelength range was chosen because it corresponds to a 'flat' portion of the

1566   spectrum for materials in these CRISM images (i.e., there are no strong absorption

1567   features within this range).

1568   Gaussian mean (band center), standard deviation (band width), and

1569   amplitude (band strength) are allowed to vary within user-defined ranges. The

1570   Gaussian fits for at least 10 individual pixels are inspected for each image to ensure

1571   that the model fits are appropriate and residuals values for the spectral fits are

1572   reported for every pixel.

1573

1574   *1.2 Field Observations*

1575 The ASD FieldSpec 3 collects reflected radiation through a fiber optic cable

1576 that is connected to three detectors within the spectrometer housing. The bare fiber

1577 optic cable has a field of view (FOV) of ~25° but can be equipped with different

1578 foreoptics to reduce the FOV to as small as 1°. Field spectra measured at Rio Tinto

1579 using solar radiation were acquired using a 5° FOV foreoptic with a typical standoff

1580 distance of ~1 m from the target of interest. The contact probe uses an internal

1581 quartz-tungsten-halogen (QTH) bulb for illumination and measures a spot size of

1582 ~10 mm. The contact probe has the advantage that viewing/illumination geometry

1583 is fixed and thus identical for all measurements.

1584

1585 *1.3 Laboratory Reflectance Measurements*

1586 The light source for the laboratory reflectance measurements with the ASD

1587 FieldSpec consisted of an enclosed QTH bulb in combination with a fiber optic cable

1588 that has a 25° FOV. The source fiber was positioned to have a central incidence angle

1589 of 30° (from normal) and the receiving fiber (attached to the spectrometer) was

1590 positioned to have a central emergence angle of 0°. The heights of the fibers were

1591 adjusted as needed in order to fully illuminate and capture the entire sample in the

1592 field of view.

1593

1594 *1.4 XRD Measurements and Rietveld Modeling*

1595 The D2 Phaser is equipped with a low voltage Cu source and a Lynxeye 1-D

1596 detector. Measurements were made using a 0.6mm divergence slit, 3 mm

1597 antiscatter shield, 2.5˚soller slit and Ni filter and rotating stage (15 rpm).

1598   The Rietveld modeling incorporated instrumental parameters included the

1599 Cukα5_Berger emission profile, a 3rd order Chebyshev polynomial (background

1600 modeling), and specimen displacement correction. Strain and crystallite size

1601 broadening were varied to help fit the peak breadths while unit cell parameters and

1602 cation occupancies within each crystal structure were refined to model the

1603 appropriate peak position. A spherical harmonics correction was also applied to

1604 correct for any intensity variations due to preferred orientation during sample

1605 mounting.

Mineral	Source
Chlorite	Zanazzi et al. (2007)
Goethite	Yang et al. (2006)
Gypsum	Boeyens and Ichharam (2002)
Illite	Gaultieri (2000)
Jarosite	Basciano and Peterson (2007, 2008); Scarlett et al. (2010)
Muscovite	Birgatti et al. (1998); Birle and Tettenhorst (1968)
Pyrite	Bayliss (1977)
Quartz	Levien et al. (1980)

1606
1607 **S Table 1:** Structure file references for the Rietveld refinement.
1608 **References:**

1609 Basciano, L.C., Peterson, R.C., 2008. Crystal chemistry of the natrojarosite-jarosite and natrojarosite-
1610   hydronium jarosite solid-solution series: A synthetic study with full Fe site occupancy. American
1611   Mineralogist 93, 853–862. doi:10.2138/am.2008.2731
1612 Basciano, L.C., Peterson, R.C., 2007. Jarosite hydronium jarosite solid-solution series with full iron site
1613   occupancy: Mineralogy and crystal chemistry. American Mineralogist 92, 1464–1473.
1614   doi:10.2138/am.2007.2432
1615 Bayliss, P., 1977. Crystal structure refinement of a weakly anisotropic pyrite. American Mineralogist 62,
1616   1168–1172.
1617 Birle, J.D., 1968. Refined Muscovite Structure. Mineralogical Magazine 36, 883–886.
1618   doi:10.1180/minmag.1968.036.282.24
1619 Boeyens, J.C.A., Ichharam, V.V.H., 2002. Redetermination of the crystal structure of calcium sulphate
1620   dihydrate, CaSO4 · 2H2O. Zeitschrift für Kristallographie - New Crystal Structures 217.
1621   doi:10.1524/ncrs.2002.217.jg.9
1622 Brigatti, M.F., Frigieri, P., Luciano, P., 1998. Crystal chemistry of Mg-, Fe-bearing muscovites 2M1.
1623   American Mineralogist 83, 775–785.
1624 Gualtieri, A.F., 2000. Accuracy of XRPD QPA using the combined Rietveld–RIR method. Journal of
1625   Applied Crystallography 33, 267–278. doi:10.1107/S002188989901643X
1626 Levien, L., Prewitt, C.T., Weidner, D.J., 1980. Structure and elastic properties of quartz at pressure.
1627   American Mineralogist 65, 920–930.

1628 Ransom, B., Bennett, R.H., Baerwald, R., Shea, K., 1997. TEM study of in situ organic matter on
1629   continental margins: occurrence and the "monolayer" hypothesis. Marine Geology 138, 1–9.
1630   doi:10.1016/S0025-3227(97)00012-1
1631 Scarlett, N.V.Y., Grey, I.E., Brand, H.E.A., 2010. Ordering of iron vacancies in monoclinic jarosites.
1632   American Mineralogist 95, 1590–1593. doi:10.2138/am.2010.3591
1633 Yang, H., Lu, R., Downs, R.T., Costin, G., 2006. Goethite, α-FeO(OH), from single-crystal data. Acta
1634   Crystallographica Section E Structure Reports Online 62, i250–i252.
1635   doi:10.1107/S1600536806047258
1636 Zanazzi, P.F., Montagnoli, M., Nazzareni, S., Comodi, P., 2007. Structural effects of pressure on
1637   monoclinic chlorite: A single-crystal study. American Mineralogist 92, 655–661.
1638   doi:10.2138/am.2007.2341
1639